Analysis of predictive models for correlation of irradiation effects on pressure vessel steels

Martin Lundgren

June 27, 2010

Abstract

The reactor pressure vessel steel of a nuclear power plant is subjected to fast neutron induced embrittlement. More specifically, hardening nanofeatures are produced within the materials by the neutron bombardment, which is of importance for the toughness of the material. The decrease in toughness is characterized by the change in ductile to brittle transition temperature.

A number of predictive semi-empirical models, for evaluation of the transition temperature shift, ΔT, have been compared, considering the Ringhals units 3 and 4 base metal data. The US Regulatory Guide 1.99 Revision 1, followed by the French FIM and Miannay formulas, is found to best agree with the results for all Ringhals units 3 and 4 base materials.

The transition temperature shift is found to follow a high exponent ($\gtrsim 0.5$) fluence behavior, and lacks a significant saturation effect. This conclusion is drawn both from the comparison of semi-empirical models, and from calculations by the least squares method.

An effect of the copper content on ΔT is clear for the base metals. Also, next to Cu, analysis indicates strongest ΔT correlations with manganese, considering elemental contents of impurities and alloying elements in the materials. When also the weld metals are taken into account, this effect becomes more pronounced and is found to follow the same behavior as among base materials. While correlations between the data and manganese are strong, effects of nickel and other elements remain uncertain.

Comparing data among Ringhals unit 2 materials, an effect of the neutron flux is noticeable. Here, half the samples are subjected to a twice as large neutron flux, and display higher temperature shifts, compared to the other half.

It needs to be noted that the database is rather small, i.e. fourteen and nine discrete data points for the base- and weld metals, respectively. Hence, all results are of poor significant quality and additional effects may be recognized when further data is added.

Keywords: Neutron irradiation, RPV embrittlement, surveillance programmes, matrix features, CRP, MNP, ductile, brittle, transition temperature shift, Charpy-V notch impact testing, neutron fluence, flux, PERFECT.

Acknowledgements

I would like to thank Jenny Roudèn at Ringhals for extensive help and advice concerning both the analysis of data and the report itself. Also, Anders Nordlund at Chalmers for many useful remarks and suggestions throughout the process.

I would also like to thank Pål Efsing at Vattenfall for giving me the opportunity to take part in this project and finally the whole staff at "material and analytical services" at Ringhals for their warm welcome.

Gothenburg, June 2010

Martin Lundgren

Abbreviations

PWR Pressurized Water Reactor

BWR Boiling Water Reactor

RPV Reactor Pressure Vessel

PKA Primary Knock-on Atom

SKA Secondary Knock-on Atom

SIA Self Interstitial Atom

MD Molecular Dynamics

MF Matrix Feature

CRP Copper Rich Precipitate

MNP Manganese Nickel rich Precipitate

DBTT Ductile-Brittle Transition Temperature

ASTM American Society for Testing and Materials

USE Upper Shelf Energy

LSE Lower Shelf Energy

Contents

1 Introduction

There are currently three pressurized water reactors (PWR's) in operation in Sweden, all of which are situated at Ringhals. These - units 2, 3 and 4 - began operation in 1975, 1981 and 1983, respectively.

The structural integrity of the reactor pressure vessel (RPV) is an essential part of the safe operation of any nuclear power reactor. Apart from a number of operational limits, various in-service inspections and maintenance procedures, surveillance programmes regarding the degradation of the RPV materials are needed. This latter issue is of particular interest for ageing management as designed end of lives for older plants are due to expire and plant life extension needs to be considered. In Sweden no operating licence limits exist, however material degradation still needs to be studied and safety issues assessed.

The main cause of RPV embrittlement is the interaction of fast neutrons with the vessel material. Specifically the time-integrated neutron flux, i.e. fluence, generally determined at the RPV inner wall, along with the impurity and alloying element contents of the RPV material itself is of particular significance. The effects on the mechanical and structural properties of neutron irradiation on RPV materials have been recognized and investigated since the early 1950's. A number of guides and models, taking various elemental concentrations into account, which evaluate the embrittlement dependence of fluence, exist. All of these have been developed on the basis of surveillance test results from commercial and/or test reactors [1].

1.1 The Company

Ringhals is the largest nuclear power plant in Sweden, roughly producing 20% of the electrical power in the country. Located on the west coast, sixty kilometers south of Gothenburg, it is one of few power plants in the world containing both boiling water reactors (BWR's) and PWR's, namely one of the former and three of the latter. Apart from the operation of the reactors, also a significant amount of research and development is performed here and at Ringhals subsidiary Barsebäck Kraft AB. The company is owned by Vattenfall and E.ON to 70.4% and 29.6%, respectively, and has some 1600 employees [2].

1.2 Background

The first reactor at Ringhals was taken into operation in 1975 and the fourth and last reactor began operation in 1983. Since design lives of nuclear power plants are typically in the range of 30-40 years, lifetime extension has become of interest. This requires that nuclear power plant engineers demonstrate by analysis, trending, equipment and system upgrades, testing and ageing management that the plant will operate safely even beyond the, upon design expected, end of life [3].

A crucial part of the analysis is the assessment of the RPV integrity, specifically to estimate the risk of RPV failure due to brittle crack propagation in the material. Regarding this issue, the main focus lies on the so called beltline region, where the neutron flux is significant. This region contains both weld- and base metals (i.e. forged base metal courses welded together by the weld metal). Since these are fundamentally different in fabrication method and material composition, both need to be studied individually. The

cylindrical part of the Ringhals 3 and 4 RPV's consist of base materials in three sections - upper, intermediate and lower shell courses - welded together by the weld material. Among the shell courses, only the intermediate and lower lie in the beltline region, which is the region containing the fuel. Materials located in this region are thus exposed to significant neutron irradiation, and only intermediate and lower shell course materials are hence included in the study. Since the base material element composition may vary between the shell courses a total of four different materials need to be considered for the Ringhals 3 and 4 reactors base material.

1.3 Purpose Of The Thesis

The goal of the report is to investigate the embrittlement predictions in Ringhals reactors 3 and 4 RPV base material due to neutron irradiation. The material embrittlement, or decrease of toughness, is generally investigated by the change in the ductile to brittle transition temperature. Currently, measured transition temperatures from Swedish RPV's are compared to, and predicted with the US Regulatory Guide Revision 2. The goal of the report is to compare Ringhals units 3 and 4 base metal transition temperature data to a number of different predictive models.

The change in the transition temperature is here calculated from experimental impact test results and compared to a number of existing predictive models, employed in different countries. Models are appreciated by calculating the (sum of squared) residuals to the measured data points.

Dependance on factors such as neutron fluence, chemical composition and flux are also investigated. For this task data from Ringhals 2 base- and weld metals and Ringhals 3 and 4 weld metals is included in the study.

1.4 Outline

The report is structured in a number of sections. Firstly, under the theoretical section, the current understanding and theory of neutron induced irradiation damage at the nanoscale will be described. Then it is qualitatively explained how such damage is manifested in the mechanical properties of materials, and how the effect is quantified and studied in nuclear power plants. A number of predictive models for evaluation of the embrittlement exist. Modeling of embrittlement in general, and specific semi empirical models, are also presented in this section.

Next, the method section treats how the results from surveillance programmes are analyzed in order to quantify the embrittlement. Specifically, how the transition temperature shift is calculated from impact testing data. Also, general methods for evaluation of results are presented here.

The results and discussion section includes the calculation of transition temperatures - the measure that will be used consistently for all analysis - and possible errors in these. Then the different, presented semi-empirical models are compared. Also, conclusions regarding effects of material composition, fluence and flux are presented and discussed. Finally, following the references, additional results and figures not included in the preceding sections are shown in the Appendix.

2 Theoretical Section

The current understanding of neutron irradiation embrittlement at the nanoscale is based on a combination of microstructural/microchemical studies and physical models. Methods for material studies include: small angle x-ray and neutron scattering, various electron microscopy techniques (TEM, SEM), atom probe microscopy and positron annihilation spectroscopy. The evolution of irradiation induced defects are predicted by thermodynamic-kinetic models. The following sections give a description of the origin and nature of irradiation induced nanofeatures and why these are of importance for material toughness at the macroscale.

The ductile to brittle transition temperature shift, ΔT, used to quantify the embrittlement, will be defined. The most widely used semi-empirical models, relating ΔT to various parameters of interest are also presented.

2.1 RPV Embrittlement - The Physics

The nano-scale features responsible for the embrittlement are generally considered to be two-fold:

Matrix Features Defect clusters within the material lattice (containing $\sim 30\%$ Fe, [4]). Primarily vacancy-solute clusters or their solute remnants.

Precipitates Distinct phases consisting of alloying- and/or impurity elements. Mainly Copper-rich and/or Manganese/Nickel rich, depending on material composition.

The origin and nature of these will be explained below.

In materials under neutron irradiation, the lattice is constantly being bombarded by neutrons. Upon initial collision between the neutrons and the atoms contained in this lattice, energy is transferred to the so called primary knock-on atoms (PKA's). Should the transferred energy exceed the displacement threshold energy, E_d (e.g. for pure iron, Fe, $E_d = 40eV$ [5]), of the atom, the PKA will escape it's lattice site and start moving through the material. The displaced PKA's are slowed down through a series of collisions with additional lattice atoms, so called secondary knock-on atoms (SKA's). Similarly the SKA's can be displaced and slowed down by the same process, causing tertiary knock-on atoms and so on. A cascade of displacements is thus produced. Each displacement can be pictured as a Frenkel-pair, i.e. one vacancy and one self-interstitial atom (SIA), see figures 1(a) **a** and 1(b) **d-e**. However, once the energy of the PKA has been dissipated through the lattice, to a value below E_d, most of the created vacancies and interstitial atoms will annihilate with each other, resulting in only a few defects. Typically, this leaves a vacancy rich core surrounded by an SIA shell in the cascade region. Furthermore, due to thermal relaxation within the pico-second-range, the total number of surviving dislocations will be additionally decreased. The course of events is shown in figure 1(b) **a-c**, as simulated by Molecular Dynamics (MD) calculations in pure iron. Alloying elements and impurities do not significantly affect the formation or recombination of displacement cascades, compared to the case of a pure-iron-material, according to current understanding among experts [6]. Simulations on pure iron are therefore believed to be representative also for real RPV materials.

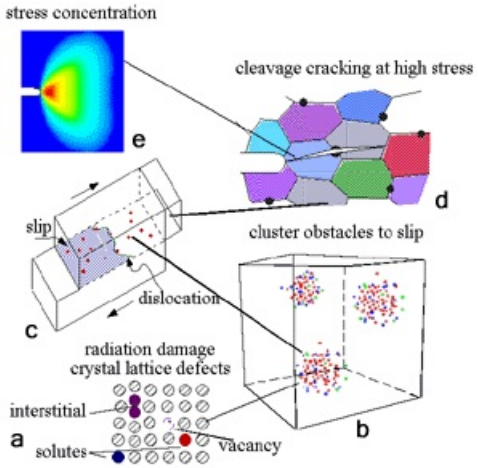

(a) Schematic figure of the embrittlement processes: **a** Primary irradiation damage to lattice; **b** residual nanofeatures: solute and defect clusters; **c** obstruction of dislocation motion by nanofeatures; **d** cleavage fracture due to hardening by nanofeatures; **e** stress concentration.

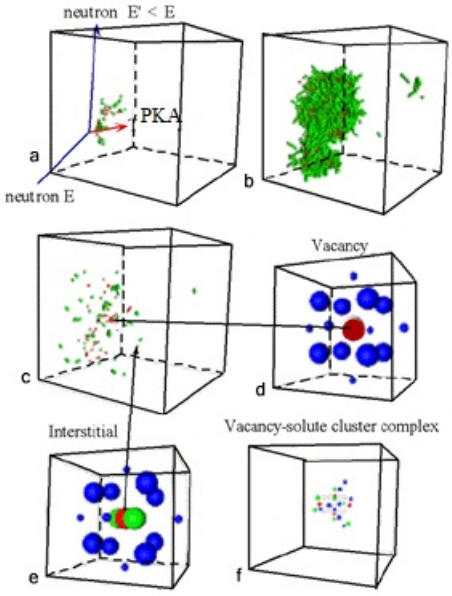

(b) Illustration of neutron induced lattice damage: **a** Neutron producing PKA damage; **b** resulting cascade and sub cascades; **c** surviving defects after vacancy-interstitial annihilation; **d** vacancy in lattice; **e** SIA in lattice; **f** residual vacancy-solute cluster after long-range diffusion.

Figure 1: Figures taken from [7].

It is in figure 1(b) shown how a large number of SIA's and vacancies are initially produced, within the so called cascade region, and are hereafter rapidly relax, whereby a large number of Frenkel-pairs annihilate and only a few defects survive. It is the migration of the surviving point defects (SIA's and vacancies) that are responsible for the embrittlement, rather than the atomic rearrangements produced in the displacement cascades. Accelerated by the irradiation itself, defects will diffuse to form clusters, interact with different solutes and impurities present in the material etc.

The residual damage is believed to be due to clustering of vacancies with various solute atoms or their solute cluster remnants, so called matrix features (MF's), or due to precipitation of solutes, forming distinct solute phases within the material.

2.1.1 Matrix Features

Solutes have a tendency to bind to the vacancies induced in the primary damage stage (especially copper, Cu, atoms). After irradiation the distribution of solute atoms will therefore no longer be random. Rather, vacancies and solutes form nanometer scale clusters within the lattice. Atom probe microscopy studies have revealed these clusters to be diluted in terms of solute atoms (they will contain a high Fe concentration), wherefore they are often referred to as "clouds" or "atmospheres". This dilute nature separates MF's from the (almost) pure solute phases known as precipitates. Exactly why the clouds do not collapse into a "real" precipitates is not yet understood, but has been suggested to be due to the high vacancy concentration within the clusters.

During the long-range diffusion, single vacancies, SIA's and small clusters diffuse long distances relative to the size of the initial cascades, a process in which MF's may grow. In low Cu steels ($Cu \lesssim 0.1wt\%$) this is the main cause of embrittlement [8]. The ductile to brittle temperature shift, which is explained below, is in such cases established to follow a square root of fluence law, $\Delta T \sim \phi^{0.5}$. Definitions of low Cu steels vary, but generally thresholds are considered to lie between $\sim 0.05 - 0.1wt\%$.

The formation of vacancy-Cu clusters within the lattice matrix has been predicted through Molecular Dynamics simulations. Manganese (Mn) and nickel (Ni) atoms are found to agglomerate around a core region with higher Cu concentration. This process reduces the total surface energy of the cluster. Mn and Ni can thus be regarded as catalysts for the MF forming process, and the number density of vacancy-solute clusters are hence found to increase with increasing Mn, Ni contents in the material [4, 6].

2.1.2 Precipitates

More important to the embrittlement in western LWR's with high Cu contents, is the precipitation of solutes (e.g. Cu, Ni, Mn, Si). More precisely, this means that solute atoms are ejected (precipitated) from the lattice, forming particles of a distinct material phase or a mixture of solute phases. The excess concentration of vacancies, due to irradiation, mainly results in the formation of copper rich precipitates (CRP's) or manganese-nickel rich precipitates (MNP's), if the levels of respective elements are sufficiently high in the material.

The evolution of the precipitates is qualitatively explained through the concept of radiation-enhanced diffusion. Due to irradiation, the material will have an increased concentration of vacancies, enhancing the diffusion of solutes, compared to the simple thermally driven diffusion. A given alloying/impurity element atom is more likely to have a nearest neighbor vacancy, compared to an unirradiated material, and the material will thus experience a higher vacancy-solute exchange rate. When the diffusing solute atom encounters another solute atom they bind together, reducing their effective energy. The precipitates may continue to grow until the solute is depleted from the lattice. Because there is a strong interaction between Cu, Ni and Mn, observed precipitates are often a mixture of CRP's and MNP's i.e. Mn-Ni precipitates with a small Cu rich core ($> 80-90\%$ Cu in the core [4]). In very Cu-low steels, distinct MNP's are observed only at high fluence levels. Since these phases may require a small degree of Cu precipitation to catalyze their nucleation, they may not contribute to hardening and embrittlement until relatively high fluences. This is often referred to as a "late blooming effect". This effect is however not completely understood and is currently an extensively discussed subject.

When modeling irradiation embrittlement the behavior due to MF's and precipitates are sometimes separated. However, the causes, character and consequences of MF's are not as well understood as those regarding CRP's and MNP's [7].

2.1.3 Ductile/Brittle Transition

The formation of displacements, MF's and precipitates by neutron irradiation is described above. Why these are of importance for the mechanical properties of the material will be qualitatively explained below.

At low temperatures or at very high strain rates metals can become brittle. This is true mainly for bcc crystals, whereas fcc metals generally remain ductile even at low

temperatures. This is because for bcc metals the number of mobile crystallographic planes are, at low temperatures, too few to allow plastic material deformation. The typical ductile to brittle behavior is sketched in figure 2.

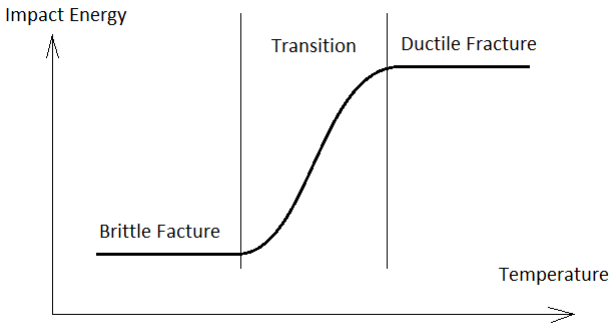

Figure 2: Ductile/Brittle behavior in metals.

By ductile behavior is meant the ability of the material to deform plastically. Plastic deformation occurs by movement of dislocations within the material. Naturally this requires an energy, e.g. an applied stress to the material. The stress required depends on the atomic bonding, crystal structure and on different obstacles such as grain boundaries, precipitate particles, other dislocations, etc. Depending on the stress needed to move dislocations, either plastic flow (ductile failure) or crack propagation (brittle failure) will occur. Whichever process requires the least energy will be favored.

At higher temperatures the yield strength is lower than at low temperatures but an eventual crack propagation will be more ductile in the former case. This means that the propagation will be accompanied by a large amount of plastic deformation, an energy consuming process. The behavior can be qualitatively understood considering atomic vibrations. As the temperature is increased in a material, so is the amplitude and frequency with which an atom vibrates. The probability for an atom to overcome the displacement energy E_d, and jump to a new lattice site, is thus increased. As stress is applied to the material the atoms will begin to slip through the lattice, forming bonds in new places. This "slippage" is macroscopically observed as a plastic deformation. In the case of a colder, more rigid lattice, the slippage does not occur and the atoms rather break their bonds, producing a crack along specific lattice planes. Also impurities, such as defects, will act as obstacles to this slippage, and dislocation motion will be "pinned" at these locations. Introduction of such obstacles renders the nature of the fracture more brittle, see figure 1(a). Similarly, increasing the number of obstacles requires a larger applied stress for the material to yield, as manifested by increasing material hardening. A ductile fracture is easily identified by the characteristically rough fracture surface, produced through plastic flow, whereas a brittle fracture produces a relatively flat fracture surface.

In between the ductile and brittle temperature plateaus (see fig. 2) is a small transition zone. In this interval the material displays characteristics of both types of fracture. For very pure materials the transition can be almost sudden, while it occurs over a range of temperatures for materials with impurities. As the amount of impurities increase, which act as obstacles to the mentioned slippage, the transition temperature range is increased.

Once a crack is initiated, its propagation will differ greatly between brittle and ductile materials. In the latter case cracks move slowly and are accompanied by a large amount of plastic deformation. Such a crack will generally not extend unless an increased stress is applied. For brittle materials cracks will, once initiated, continue to grow, even if stress is not increased. Naturally, for RPV steels the former process is preferred.

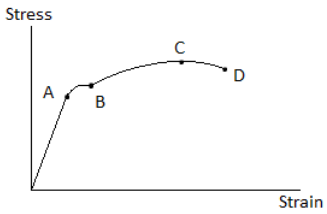

(a) Typical stress/strain behavior for steels.

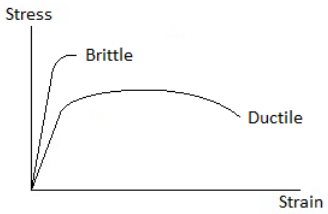

(b) Comparison brittle/ductile materials.

Figure 3: Deformation occurs in a material as a load is applied. Stress is the internal force per unit area as experienced by the material, while the strain is the unit change in deformation/elongation of the specimen.

Figure 3(a) shows the typical stress-strain behavior for a normal steel. A is called the proportional limit, simply because the material exhibits a linear behavior up to this point. Beyond limit A the elongation increases more rapidly and at B a sudden elongation occurs without having to increase the applied stress significantly and the material is permanently deformed. Below B, the yield strength, the material is elastic and removal of the applied stress results in the material returning to its original condition. Stress continues to increase due to hardening up to point C, which is termed the ultimate tensile strength. Hereafter the stress decreases until the material fractures at D. Figure 3(b) shows the difference between brittle and ductile metals. Brittle materials experience very little plastic deformation and fracture almost instantly beyond its elastic limit. The potential energy of a deformed specimen is given as the area under the curve, e.g. figure 3(a). Up to the proportional limit this is simply, in analogy with a simple linear spring, $E = \frac{kx^2}{2}$, where k is the slope of the linear curve and x is the elongation relative to the equilibrium position (strain). For an arbitrary point on the curve, the energy relative to the equilibrium position is given as the integral (area) of the curve. The total fracture energy is therefore given as the total area under respective curve. It is thus seen that although a brittle material generally displays a higher yield strength, a larger quantity of energy is needed to fracture a ductile specimen.

Since the transition zone ranges over an interval of temperatures no single definition of a specific ductile-brittle transition temperature (DBTT) can be defined. In impact testing applications it is often taken as the temperature at which the energy needed to fracture the specimen corresponds to 41 J, or 68 J. The former value will be employed throughout this study. Figure 4 shows how ΔT_{41J} is determined from the ductile-brittle transition curves.

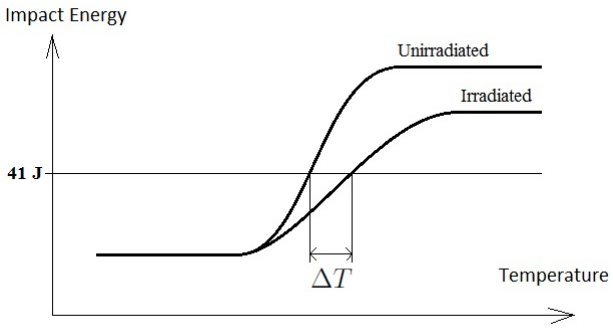

Figure 4: The change in transition temperature shift, as defined at 41 J.

2.2 Surveillance Programmes

The surveillance programmes of RPV's are designed to follow the degradation of plant specific materials due to neutron irradiation. The area surrounding the core (the so called beltline region) is the most critical region of the RPV, since the neutron flux intensity peaks here. Naturally, this region is the one of main interest. By testing of encapsulated RPV material specimens, placed and irradiated just outside the core barrel, the integrity can be assessed. Surveillance capsules are suggested to be positioned within the reactor vessel so that the specimen is subjected to the same, as closely as possible, physical environment as the RPV wall, e.g. neutron spectrum and temperature history.

Specifically, Ringhals unit 3 and 4 were both supplied with 6 capsules, each with 72 Charpy, 9 tensile and 18 compact tension surveillance specimens. All were mounted in the reactors, in the geometry shown in figure 5(a) upon construction and are extracted hereafter. Since there is a 45^o angular symmetry in the core, the six capsule positions indicated in figure 5(a), are essentially only two, namely at 17^o (U,V and X) and 20^o (W, Y and Z).

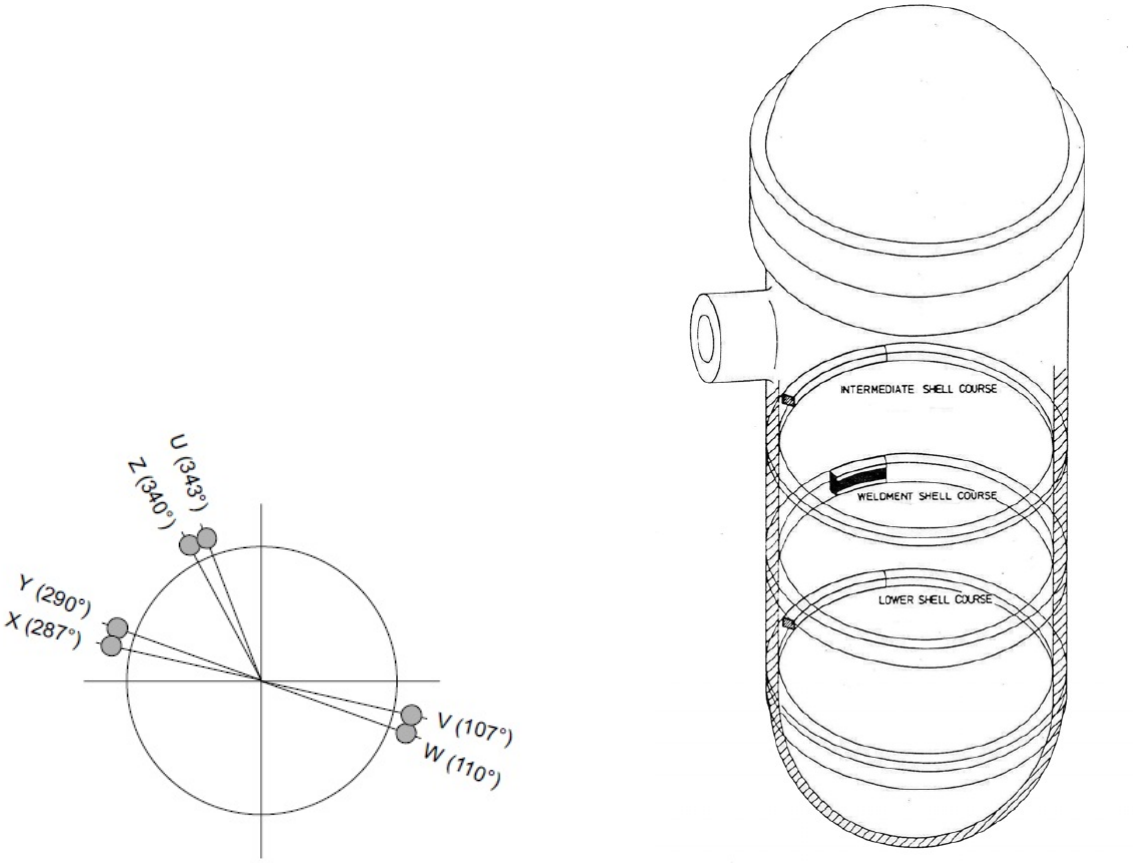

(a) Position of specimen capsules in Ringhals 3 and 4.

(b) Location of materials from different shell courses.

Figure 5: Figures taken from [9].

The angular positions of capsules in Ringhals 2, on the other hand, are of greater variation. These are situated at 15^o, 25^o, 35^o and 45^o. Specimens hereof are of importance for studying the effect of flux, as will later be described.

The RPV itself is constructed in sections, called shell courses, which are welded together. These sections, and the weld material itself, vary in composition, fabrication method, structure etc. and must hence all be inspected. Each capsule contains 18 Charpy-specimens from the weld metal, lower- and intermediate shell course base metals, and from the so called heat affected zone, which is the base metal layer subjected to heating due to the welding procedure. This latter material is specifically studied since its metallographic structure has significantly altered by the heat input from the welding operation, but it is not of interest in this particular report. The position of respective material is indicated in figure 5(b). The status of each capsule is shown in table 1. Capsules removed in 2007 are currently under evaluation and are thus not included in the report. Radially, all capsules are located closer to the core than the vessel wall, in order to achieve an accelerated exposure of specimens, so that their condition, upon removal from the reactor, may represent the RPV material at a later time of life. The accumulated flux in a specimen is related to the maximum fluence at the RPV wall through the "lead factor", which is simply the ratio of these two.

Table 1: Status of capsules.

Capsule designation	Ringhals 3	Ringhals 4
U	Removed in 2000	Removed in 1999
V	Removed in 1984	Removed in 1991
W	Removed in 1996	Removed in 2007
X	Removed in 2000	Removed in 2007
Y	Removed in 2007	Removed in 1999
Z	Removed in 2007	Removed in 2007

2.2.1 Sample testing procedures

Until present date, Studsvik Nuclear AB has been accredited to perform all surveillance testing of irradiatied RPV steels in Sweden. Capsules are to be withdrawn according to a predetermined, approved schedule and specimens must be tested and the results and corresponding analysis reported within a year from removal.

Of the three different types of surveillance specimens presented above, only "Charpy" are of interest for this report. The Charpy-V testing is performed in an impact machine, such as a "swinging axe pendulum". Samples need to be of regular geometry and pre-notched, see figure 6.

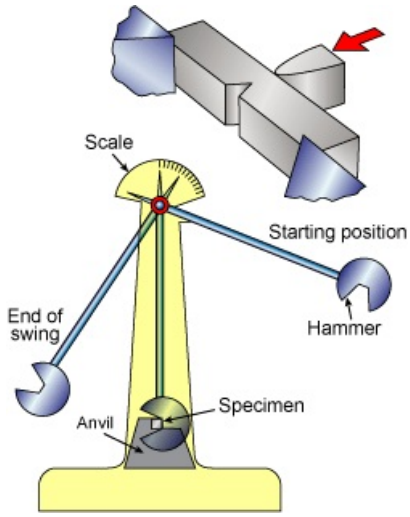

Figure 6: Schematic of Charpy swinging axe pendulum and Charpy specimen. Figure taken from [11].

Dimensions are, by ASTM standards, 55x10x10 mm, with a 45^o v-shaped notch, 2 mm deep. The sample is fractured, and the energy needed for the fracture is determined. By performing this procedure for a number of identically irradiated specimens, while varying temperature, the ductile/brittle transition can be investigated. This is initially conducted for approximately 6-8 specimens over a wide temperature range, and the remaining specimens are tested at the region of interest, i.e. the transition region. The programme includes testing of the unirradiated material for usage as a reference.

Results from such testing are used, by ASTM standard, to fit a hyperbolic tangent curve, whereby a transition temperature can be determined. This procedure is described

in the method section.

Also tensile tests included in capsules may be used to establish the stress-strain behavior (e.g. figure 3) of irradiated specimens.

2.2.2 Fluence determination

In order to relate the accumulated flux (fluence) induced in surveillance specimens to that at the RPV wall, one must know how the flux varies between these regions of interest. Basically, the general rule of thumb is that the flux, and thus also fluence, decreases with distance from the reactor core.

In order to measure the fluence (mainly fast, $E > 1MeV$, as will be described in the following section), to which surveillance specimens are subjected to, dosimeters are included in each capsule. These are of two kinds [10]:

1. Non-fission dosimeters; materials such as iron, nickel, copper and aluminium-cobalt of high purity, often in the form of metal wires, which transmute into other metals upon neutron irradiation. The concentrations of these serve as a measure of the neutron fluence received by respective dosimeter.

2. Fission dosimeters; e.g. neptunium 237 oxide and uranium 238. By evaluating concentrations of fission products the fluence can be determined. This can potentially give a different measure of the fluence than in case 1, since the threshold energies for fission can be chosen lower (or higher) than those for transmuting the metals, by usage of appropriate fissile material. Hence, by knowledge of the different thresholds for these nuclear reactions, information regarding the neutron spectrum can be derived.

The fluence is also calculated using computer codes, and compared to the dosimeter results. Traditionally at Ringhals, this has been done with multigroup transport theory in an R, Θ geometry. Specifically, the activation of dosimeter materials is calculated and compared to the measured activation of the same. Calculated fluences at the vessel wall are related to those of the surveillance specimens through lead factors. The lead factor is defined as the ratio of exposure of the surveillance specimens to the highest anticipated exposure at the RPV wall. By ASTM standards surveillance capsule lead factors are recommended to be in the range of one to three [6].

2.3 Modeling

The majority of formulas developed within various surveillance programmes aim to correlate the DBTT shift (ΔT) with different parameters: neutron fluence, irradiation temperature, chemical composition, neutron flux, neutron spectrum, microstructural state, etc. Some general features regarding these parameters, described in [12], are stated below.

Neutron Fluence The neutron fluence is obviously a major factor for the embrittlement. However, it is generally deemed that the neutron efficiency for creating damage decreases as the fluence increases. The reason for this is, as explained in the RPV embrittlement section, impurity/alloying elements will be precipitated as fluence is increased. These will thus be depleted from the lattice matrix or locally concentrated within it and

the effect of further neutron bombardment is decreased. In other words, ΔT versus fluence, ϕ, should demonstrate a steeper slope for low fluences than for higher. In many cases this behavior is modeled using a power law: $\Delta T \sim \phi^n$, where the exponent n is a number less than one.

A lower fluence threshold for observing neutron induced embrittlement is generally deemed to be approximately $\phi = 1 \cdot 10^{18} n/cm^2$ $(E > 1MeV)$ [13].

Irradiation Temperature Also, the temperature at which the material of interest is irradiated, is important. As previously stated many of the initially created Frenkel pairs are thermally relaxed and annihilate. Also, this parameter is of importance for the evolution of defects, especially MF's. Intuitively, this suggests that usage of a higher irradiation temperature should result in less irradiation embrittlement. However, most PWR's operate in the range $250^oC - 300^oC$ and in a given country all pressurized reactors have the same temperature, more or less. The temperature dependence is therefore generally not explicitly introduced in the models.

Chemical Composition The chemical composition of the steel serves as an important parameter in the design of models. Especially copper, nickel and phosphorous (Cu, Ni, P) have been identified as major contributors to the embrittlement process. Although not completely understood, experiments show that irradiation accelerates precipitation of Cu, in synergy with Ni and also manganese (Mn) as recently found in [14], in small particles which harden the steel. The effect of P is similar to that of Cu as phosphides are precipitated during irradiation. Intergranular precipitation of P may however result in a non-hardening embrittlement. In other words both material yield and toughness will be decreased, whereas the effect of other elements regarded generally increases the yield strength. The effect of P is important mainly in eastern WWER type steels where levels hereof are generally higher than in western RPV materials. Some synergism with Ni supposedly exists also for P [14]. Tests also show that the influence of different alloying elements and impurities is only visible above specific threshold concentrations.

Flux/Fluence Rate The question regarding flux or fluence rate is in no way trivial. It has been suggested that a higher flux might result in a higher exponent in the fluence dependence, but opinions diverge. It may have to be considered when comparing results from test reactors, where the flux is generally high ($\sim 5 \cdot 10^{12} n/cm^2 s$, $E > 1MeV$), to surveillance programme results from commercial reactor with fluxes of $\sim 5 \cdot 10^{10} n/cm^2 s$, $E > 1MeV$. Nevertheless, such trends are not completely clear and none of the models considered here explicitly take the fluence rate into account.

Neutron Spectrum As earlier discussed, only sufficiently energetic neutrons contribute to the hardening of the RPV material. The neutron spectrum at the point of interest on the RPV wall therefore needs to be considered and quantified properly to appreciate the amount of neutrons energetic enough to induce damage. It is generally accepted that neutrons of energies $> 0.1MeV$ are mainly responsible for producing the majority of the damage, but for practical reasons a number of $1MeV$ is employed throughout most of Europe. For example, a neutron of 1 MeV may transfer up to 70 keV to a PKA in pure iron [7]. Care has to be taken when comparing results from reactors with very

different sprectra, e.g. heavy water reactors, breeders etc., where usage of the unit dpa (displacements per atom) is recommended.

2.3.1 Empirical Models

The following formulas were all developed in various national surveillance programmes or from nuclear test reactor results. These are "hybrid" models, meaning that they incorporate both physically motivated features and empirical calibration. This semi-empirical nature means that the formulas are obviously not universally applicable to arbitrary materials. However, applying them on a specific material and comparing to test results may provide a basis for understanding what parameters are of importance to that specific material.

All models to be considered are presented below in the table 2, with a short description of their dependance on fluence and alloying elements.

Table 2: Summary of models to be considered. Chemical elements of importance to the model and the fluence dependence is presented.

Model	Chemical dependence	Fluence dependence
Regulatory Guide 1.99 Revision 1	P, Cu	$\phi^{0.5}$
Reg.G.Rev.2	Cu, Ni	$\phi^{0.28-0.1\log\phi}$
FIM	P, Cu, Ni	$\phi^{0.35}$
FIS	P, Cu, Ni	$\phi^{0.35}$
Miannay	P, Cu, Ni	$\phi^{0.7}$
KTA 3203	none	ϕ^{1}
JEPE	P, Cu, Ni	$\phi^{0.29-0.04\log\phi}$
PNAE	P, Cu	$\phi^{1/3}$
E 900-02 (Reg.G.Rev.3)	Cu, Ni	$\phi^{0.5076}$ and $\tanh(\log\phi)$
EONY	P, Mn, Cu, Ni	$\phi^{0.5}$ and $\tanh(\log\phi)$

A more detailed presentation of the models follows.

In USA In 1970 the first model, taking chemical composition into account, was published. From this, the **Regulatory Guide 1.99-Revision 1** was developed [15]:

$$\Delta T = \frac{5}{9}\left(40 + 5000(P - 0.008) + 1000(Cu - 0.08)\right)\phi^{0.5}, \tag{1}$$

where P and Cu denote weight percentages (wt%) for residual elements phosphorous and copper, respectively. Here, thresholds of 0.008 for P and 0.08 for Cu are employed, below which the expressions containing P and Cu are set to zero, respectively. ϕ is given in $10^{19}n/cm^2$, with n meaning neutrons.

With further analysis of US reactors surveillance data a synergistic effect of Ni with Cu was recognized, and base and weld metals were distinguished. The **Regulatory Guide 1.99-Revision 2** was issued in 1988 [16]:

$$\Delta T = \frac{5}{9}CF(Cu, Ni)\phi^{0.28-0.10\log\phi}, \tag{2}$$

where the log is the base-10 logarithm, ϕ is given in $10^{19} n/cm^2$ and $CF(Cu, Ni)$ is a chemical factor containing Cu-Ni coupling effects. CF is given in tables for base- and weld materials respectively. It is worth noting that (2) contains no dependence on P. This is because the materials contained in the database in question had a relatively low P concentration ($< 0.024 wt\%$). Also, the addition of a $\log \phi$ term in the exponent of the fluence gives a larger saturation of ΔT for high fluences and a more rapid increase for low fluences.

In France Extensive test reactor experiments conducted in France suggested a modification of the initially used US Reg. Guide 1.99-Rev.1, recognizing the Cu-Ni coupling effect. Brillaud et al. [17] derived the **FIM formula**:

$$\Delta T = (17.3 + 1537(P - 0.008) + 238(Cu - 0.08) + 191 Ni^2 Cu)\phi^{0.35}, \tag{3}$$

and **FIS formula**:

$$\Delta T = 8 + (24 + 1537(P - 0.008) + 238(Cu - 0.08) + 191 Ni^2 Cu)\phi^{0.35}. \tag{4}$$

These two models are essentially the same but whereas FIM is a direct best fit to data, FIS is more conservative, from a safety point of view. Same thresholds as for US Reg. Guide 1.99-Rev.1 apply here. Another model, derived by Miannay et al. [18], **the Miannay formula**:

$$\Delta T = \big(10.98 + 316.41P + 225.29(Cu - 0.08) + 12.10(Ni - 0.7) + 48.31(Cu - 0.08)(Ni - 0.7)\big)\phi^{0.7}, \tag{5}$$

is noteworthy because of the relatively high exponent of ϕ.

In Germany The German **KTA 3203 standard** is a temperature shift limit rather than a predictive formula. It states that the temperature shift of the maximally irradiated region of the RPV inner wall must not exceed [19]:

$$RT_{limit} = \begin{cases} 40^o C, & \phi \leq 1 \cdot 10^{19} n/cm^2 \quad (E > 1 MeV); \\ 30^o C + 10 \cdot \phi, & \phi > 1 \cdot 10^{19} n/cm^2 \quad (E > 1 MeV). \end{cases} \tag{6}$$

ϕ is given in 10^{19} n/cm^2 $(E > 1 MeV)$ and Cu, Ni need not exceed 0.15 wt% and 1.1 wt%, respectively. This "model" is very conservative and will be included only as an inspection whether determined temperature transition shifts exceed it or not.

In Japan The Japanese Embrittlement Predictive Equations (**JEPE**) were derived from surveillance results of pressure vessel steels. These recognize the effects of P, Cu and synergism between Cu and Ni. For base metals this reads:

$$\Delta T = (-16 + 1210P + 215Cu + 77\sqrt{NiCu})\phi^{0.29 - 0.04 \log \phi}. \tag{7}$$

No thresholds are explicitly given in the formula.

In Russia Vessel steels employed in Russia and Eastern Europe differ from the steels used in Western Europe, USA and Japan. The following formula will nevertheless be included for comparison with experimental data. According to Russian standards the fast neutrons, responsible for embrittlement, are defined as those with energies $> 0.5MeV$ ($1MeV$ for western standards), and fluence is given in $10^{22}n/cm^2$. For the application of this model it will be assumed that [12]:

$$\begin{array}{c} \phi \text{ in } 10^{22}n/cm^2 \\ E > 0.5 \text{ MeV} \end{array} \Leftrightarrow \begin{array}{c} 18\phi \text{ in } 10^{19}n/cm^2 \\ E > 1 \text{ MeV} \end{array} \tag{8}$$

The **PNAE G-7-002-86 formula** at an irradiation temperature of 270^{o}C is defined as:

$$\Delta T = 800(P + 0.07Cu)(18\phi)^{\frac{1}{3}}, \tag{9}$$

where ϕ is now given in $10^{19}n/cm^2$. The model pays no consideration to whether the material is weld- or base metal [20]. The guide is developed for first generation, WWER-440, Russian RPV steels. The second generation, WWER-1000, steels are generally low in Cu and P while they contain a significant amount of Ni and Mn. For such steels a model of type: $\Delta T = (aNi + bMn + c)(18\phi)^{1/3}$ has been proven to best fit results [21].

More Recent Models Due to better understanding of the embrittlement processes and broader databases of surveillance results new models are constantly being developed. The **E 900-02 model**, also known as the Regulatory Guide 1.99 Rev.3, was introduced in 2002 and is recommended by the American Society for Testing and Materials (ASTM) [6]:

$$\Delta T = (SMD + CRP) \cdot \tfrac{5}{9}, \text{ where:}$$

$$SMD = Aexp\left[\tfrac{20730}{T_c+460}\right]\phi^{0.5076}, \qquad CRP = B\left[1 + 2.106Ni^{1.173}\right]F(Cu)G(\phi)$$

$$A = 6.71 \cdot 10^{-18}, \qquad B = \begin{cases} 234, & \text{welds;} \\ 128, & \text{forgings;} \\ 208, & \text{Combustion Engineering (CE) plates.} \end{cases}$$

$$G(\phi) = \tfrac{1}{2} + \tfrac{1}{2}\tanh\left[\tfrac{\log(\phi)-18.24}{1.052}\right], \qquad F(Cu) = \begin{cases} 0, & Cu \leq 0.072wt\%; \\ (Cu - 0.072)^{0.577}, & Cu > 0.072wt\%. \end{cases} \tag{10}$$

The expression is divided in two terms, SMD and CRP. These represent the embrittlement due to matrix features and copper rich precipitates, respectively.

T_c is the coolant temperature in ^oF, Cu and Ni are the wt% of respective element and ϕ is the neutron fluence in n/cm^2. For Ringhals base material, a value $B = 128$, corresponding to forgings, will be used consistently. Maximum allowed Cu concentration in this model is 0.25 wt%, a value far greater than that of the material from Ringhals 3 and 4, as will be seen.

Yet a model was developed by Eason, Odette, Nanstadt and Yamamoto et al. [4]. This new modeling effort was motivated by further surveillance data being presented in 2003-2004, both from BWR and PWR reactors. To be able to represent data from BWR's (for

which the fast flux at the RPV wall, φ, is substantially lower than in a PWR) correctly, the notion of an effective fluence is here introduced:

$$\phi_e = \varphi t_e = \begin{cases} \phi = \varphi t, & \varphi \geq 4.39 \cdot 10^{10}; \\ \varphi t \left(\frac{4.39 \cdot 10^{10}}{\varphi} \right), & \varphi < 4.39 \cdot 10^{10}. \end{cases} \tag{11}$$

For PWR's the fast flux ($> 1MeV$), φ, is of the order $\sim 5 \cdot 10^{10} n/cm^2 s$ [12], and only the former case of equation (11) will here be considered. The formula, which will be referred to as simply the **EONY formula** consists of both a Matrix Feature (MF) term, modeling the low Cu behavior, as well as a Copper-Rich Precipitate (CRP) term to model the shift due to precipitation of Cu, P and other elements.

$$\Delta T = (MF + CRP) \cdot \frac{5}{9}, \tag{12}$$

with

$$\begin{aligned}
MF &= A(1 - 0.001718T_i)(1 + 6.13PMn^{2.47})\sqrt{\phi}, \\
A &= \begin{cases} 1.140 \cdot 10^{-7} \text{ for forgings;} \\ 1.561 \cdot 10^{-7} \text{ for plates;} \\ 1.417 \cdot 10^{-7} \text{ for welds,} \end{cases} \\
CRP &= B(1 + 3.77Ni^{1.191}) \left(\frac{T_i}{543} \right)^{1.10} f(Cu_e, P) g(Cu_e, Ni, \phi), \\
B &= \begin{cases} 102.3 \text{ for forgings;} \\ 102.5 \text{ for plates in non - CE mfg. vessels;} \\ 135.2 \text{ for plates in CE mfg. vessels;} \\ 155.0 \text{ for welds;} \\ 128.2 \text{ for SRM plates,} \end{cases} \\
Cu_e &= \begin{cases} 0 \text{ for } Cu \leq 0.072 wt\%; \\ Cu \text{ for } Cu > 0.072 wt\%, \end{cases} \\
f(Cu_e, P) &= \begin{cases} 0 \text{ for } Cu \leq 0.072; \\ [Cu_e - 0.072]^{0.668} \text{ for } Cu > 0.072 \text{ and } P \leq 0.008; \\ [Cu_e - 0.072 + 1.359(P - 0.008)]^{0.668} \text{ for } Cu > 0.072 \text{ and } P > 0.008, \end{cases} \\
g(Cu_e, Ni, \phi) &= \frac{1}{2} + \frac{1}{2} \tanh \left[\frac{\log(\phi) + 1.139Cu_e - 0.448Ni - 18.120}{0.629} \right].
\end{aligned}$$

T_i is the irradiation temperature in ^oF. Again, the interest is on the forgings, here of concern to parameters A and B. The validity of the formula is, as for (10), again restricted to a maximum value of $Cu \sim 0.3wt\%$, but has no impact on application to Ringhals materials.

It can be noted that both equation (10) and (12), as well as (1) and (2), are derived in a ^{o}F temperature scale, hence the multiplication with $\frac{5}{9}$ to convert to ^oC. The usual

subtraction with 32^oF (i.e. $[^oC] = ([^oF] - 32) \cdot \frac{5}{9}$) is neglected since ΔT is a temperature difference in which $32 - 32 = 0$, naturally. The EONY model is seen to include an effect of Mn, something all other models presented here lacks. Actually, the most dominant contribution of Mn to the EONY-model is not through the $PMn^{2.47}$ term, but through the coefficients of the equation (especially A and B, where the main difference in material composition is the Mn contents).

All models here presented are more or less "simple", in that they do not consider any secondary or parallel processes, such as the mentioned late blooming effect. Also, since the formulas are developed using specific databases and materials, test results from significantly different physical conditions may not agree well with predictions. For instance, materials with a composition very different from those in the database should not be expected to behave accordingly.

2.3.2 PERFECT

The product of the EU-project PERFECT is a multi-scale numerical software for evaluation of irradiation damage in reactor components. It is designed to simulate the physics of neutron induced embrittlement starting at the nanoscale, deriving mechanical properties of materials at the macroscale. The algorithm can be divided into a number of sub-problems:

1. As mentioned, energetic neutrons produce PKA's. A PKA spectrum can thus be derived directly from the neutron spectrum. Each PKA can, dependant of its energy, produce a displacement cascade and associated sub-cascades, resulting in a number of surviving point defects. This, the primary damage, is predicted with Molecular Dynamics (MD) codes.

2. The evolution of the residual defects (vacancies, interstitials, etc.), leading to either annihilation or clustering, is modeled with Kinetic Monte Carlo (KMC).

3. The resulting clusters are considered as seeds for the defects involved in the material hardening. These will in the long-term grow, shrink, coalesce, interact with solute atoms (impurity- and alloying elements) etc. Such behavior is in PERFECT modeled with Rate Equation Theory and other thermodynamics-based models.

4. The material hardening itself, in which dislocation motion is restrained by defects is at a first stage simulated by MD. Considering only one dislocation, forces and mobility can be derived by this method. Using these results the combined effect of a distribution of defects are studied using Discrete Dislocation Dynamics (DDD) at the mesoscopic scale.

5. Finally, the critical resolved shear stress can be computed on any slip system, from which the macroscopic yield strength can be derived.

An interatomic potential is constructed within PERFECT to simulate interactions within the lattice. Formation energies of point defects, cluster defects, binding energies of defects with solutes of alloying elements and migration energies are calculated with using Density Functional Theory (DFT), utilizing the constructed potential. More specifically, migration of SIA's, interactions of C and N with defects, interaction of solutes with vacancies and

interactions of P with vacancies and SIA's are DFT calculations of concern to PERFECT [22, 23].

3 Method

The data obtained from impact testing are discrete temperature-fracture energy data points for a specific fluence and material. How these tests are performed and how the ductile-brittle curves, as in figure 4, are constructed and the ΔT_{41J} computed, is the subject of the following section.

Also, how the results are analyzed and compared to models will briefly be discussed.

3.1 Charpy-V Notch Impact Testing

A specimen is struck by a hammer on a pendulum arm while the specimen is held at a fixed position. The hammer strikes opposite the notch and the energy absorbed in the fracture-process is determined by measuring the loss in momentum (motion) of the pendulum. By applying this test to identical specimen at different temperatures, the ductile-brittle transition becomes apparent, studying the fracture energy, E, as a function of temperature.

Since "identical" specimen are needed for the analysis, a sequence of samples are required for each material composition and fluence level.

The data obtained for a specific material and fluence is fitted according to a hyperbolic tangent function [24]:

$$E = \frac{USE + LSE}{2} + \frac{USE - LSE}{2} \tanh(\frac{T - T_0}{C}). \tag{13}$$

Here, USE is the upper shelf energy, LSE is the lower shelf energy, generally set to 2.7 J, T_0 marks the inflection point of the tanh-function and C is half of the transition temperature range from lower to upper shelf. USE, T_0 and C are regarded as parameters and fitted to the experimental data according to the least squares method. In practice this means varying the three parameters to find a minimum sum S of squared residuals:

$$S = \sum_{i=1}^{n} r_i^2 = \sum_{i=1}^{n} (y_i - f(x_i, USE, T_0, C))^2, \tag{14}$$

where (x_i, y_i) are the experimental data points (T_i, E_i), n is the total number of data points and f is the hyperbolic fit given in (13).

With all parameters known, the transition temperature T_m is determined by setting $E = 41$ J in (13).

3.2 Evaluation

Much of the discussion in this report will deal considerably with model data comparisons, fitting etc. In this context the notion of residuals, as introduced in the section above, and the least squares method are useful. A residual, r_i, is the difference between a measured value and its corresponding model estimate:

$$r_i = Measured(i) - Model(i), \tag{15}$$

where i is the data point considered. In this calculation i may refer to any recorded independent variables incorporated in the model (e.g. for the temperature shift: chemical

contents, fluence, temperature, etc.). In the least squares method the sum of squared residuals is minimized to find the best fit. It is performed exactly as in (14) but with $f(parameters)$ as the model used for the best fit.

A good model should naturally display relatively small residuals overall. Residuals in such a model should also show no obvious trends against any variable included or not included in the model. For example, if residuals are consistently large when a specific parameter is large, while they are small when the parameter is small, it might suggest a dependance on that parameter.

4 Results and Discussion

The chemical composition of the samples considered are given in table 3, [9]. Also the weld metal is included here, for reasons which will later be apparent.

Table 3: Chemical composition of surveillance probes (wt%).

	C	Si	Mn	P	S	Cr	Mo	Ni	V	Co	Al	Cu
	Base metal											
R3 Int.	0.18	0.19	0.76	0.006	0.006	0.43	0.54	0.88	<0.01	0.013	0.017	0.08
R3 Low.	0.19	0.19	0.74	0.006	0.006	0.42	0.6	0.9	<0.01	0.013	0.013	0.1
R4 Int.	0.21	0.2	0.71	0.006	0.007	0.45	0.63	0.88	<0.01	0.013	0.015	0.09
R4 Low.	0.21	0.18	0.75	0.006	0.008	0.43	0.63	0.88	<0.01	0.014	0.016	0.1
	Weld metal											
R3 Weld	0.052	0.21	1.46	0.009	0.006	0.07	0.50	1.58	0.002	0.015	0.027	0.08
R4 Weld	0.068	0.14	1.35	0.015	0.004	0.04	0.50	1.66	0.00	0.010	0.024	0.05

4.1 Calculation of transition temperatures

The experimental results for fracture absorbtion energy are taken from [9], and fitted curves for Ringhals unit 3 and 4 are shown in figures 7(a)-7(b) and 8(a)-8(b), respectively. Curves are identified from left to right with increasing fluence. Also, the 41J limit, used as reference for the ductile/brittle behavior, is indicated by the dashed line.

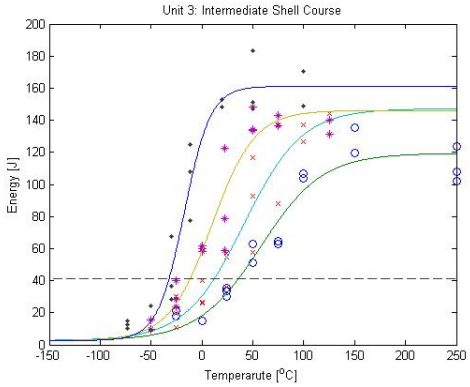

(a) Intermediate Shell Course.

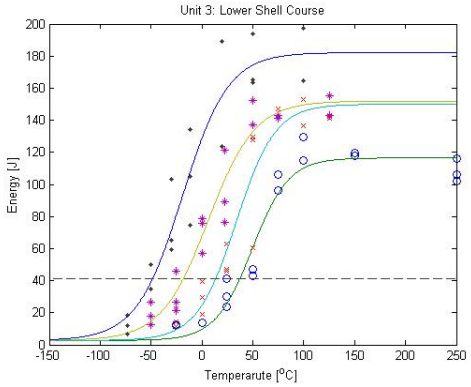

(b) Lower Shell Course.

Figure 7: Ductile/Brittle Charpy curves for Ringhals unit 3. Experimental data and fitted curves.

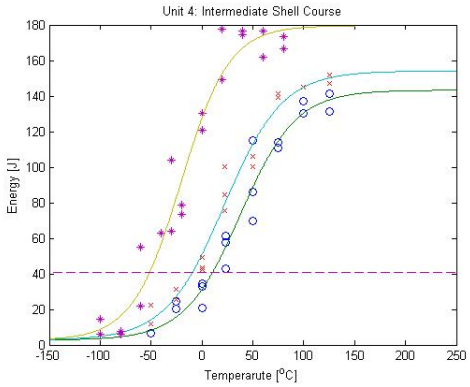

(a) Intermediate Shell Course.

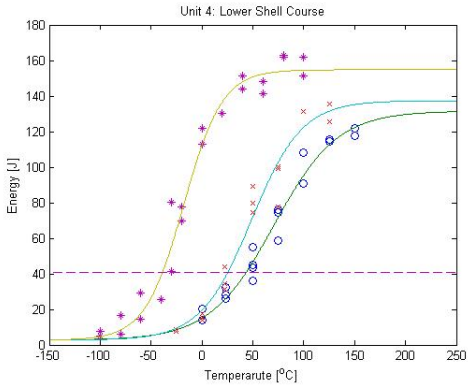

(b) Lower Shell Course.

Figure 8: Ductile/Brittle Charpy curves for Ringhals unit 4. Experimental data and fitted curves.

Table 4: Calculated transition temperature shifts and upper shelf energies for Ringhals Unit 3, Intermediate and Lower Shell Course.

Intermediate Shell Course				
Fluence·10^{19} $[n/cm^2]$ $(E > 1MeV)$	0	0.88	5	6.79
T_{41J} $[^oC]$	-32.5	-11.8	11.8	35.7
ΔT_{41J} $[^oC]$	0	20.7	44.3	68.2
USE $[J]$	161.2	146.1	147.2	119.4
ΔUSE $[J]$	0	-15.1	-14	-41.8
Lower Shell Course				
Fluence·10^{19} $[n/cm^2]$ $(E > 1MeV)$	0	0.88	5	6.79
T_{41J} $[^oC]$	-48.7	-18.5	13.4	37.0
ΔT_{41J} $[^oC]$	0	30.2	62.1	85.8
USE $[J]$	182.2	152.0	150.0	116.5
ΔUSE $[J]$	0	-30.2	-32.2	-65.7

Table 5: Calculated transition temperature shifts and upper shelf energies for Ringhals Unit 4, Intermediate and Lower Shell Course.

Intermediate Shell Course			
Fluence·10^{19} $[n/cm^2]$ $(E > 1MeV)$	0	3.61	6.91
T_{41J} $[^oC]$	-51.3	-9.2	10.6
ΔT_{41J} $[^oC]$	0	42.0	61.9
USE $[J]$	179.6	154.1	143.3
ΔUSE $[J]$	0	-43.5	-54.3
Lower Shell Course			
Fluence·10^{19} $[n/cm^2]$ $(E > 1MeV)$	0	3.61	6.91
T_{41J} $[^oC]$	-38.7	25.5	43.6
ΔT_{41J} $[^oC]$	0	64.2	82.3
USE $[J]$	154.8	137.4	131.6
ΔUSE $[J]$	0	-17.4	-23.2

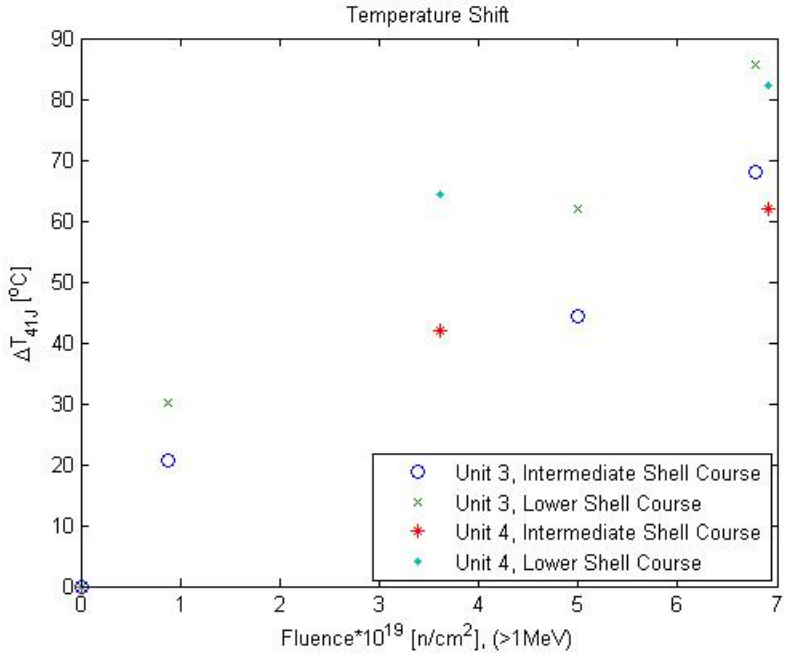

Figure 9: Determined ΔT shifts for all shell courses and fluences.

The 41J-transition temperature and USE along with associated shifts, in relation to unirradiated samples, are shown in tables 4 - 5. The transition temperature shifts, ΔT, as determined from the Charpy curves are shown with varying fluence in figure 9, for all shell courses.

It is interesting to note that the shifts displayed in units 3 and 4 lower shell courses are consistently higher than those displayed in the intermediate shell courses, for a given fluence level. A comparison between the chemical composition in table 3 shows a higher wt% of Cu in the lower shell courses compared to the intermediate ones. Furthermore, all these values lie close to the Cu thresholds, generally identified within $0.05 - 0.1wt\%$ [4]. Consequently, the accelerated embrittlement due to Cu may be present in all, none, or only the materials with the highest Cu contents.

4.1.1 Effect of measurement errors

Since the results in tables 4-5, will be used consistently throughout this report it is necessary to establish their reliability. Or rather, investigate what influence a faulty measurement may have in the calculation of ΔT. Observing the tanh-fitted curves in figures 7 and 8, ones notices a spread of data points around the fits. A large deviation from the fitted curve will naturally effect the shape, and value of ΔT, especially if the corrupt data point lies in the transition region, where the curve is steep. Taking for instance the unirradiated curve (far left one) in figure 8(a), and deleting the most deviating data point in the transition region, see figure 10. This particular curve is chosen since unirradiated curves display a larger slope in the transition region (and is hence more sensitive to errors here) and because it displays at least two potentially deviant data points within the same region.

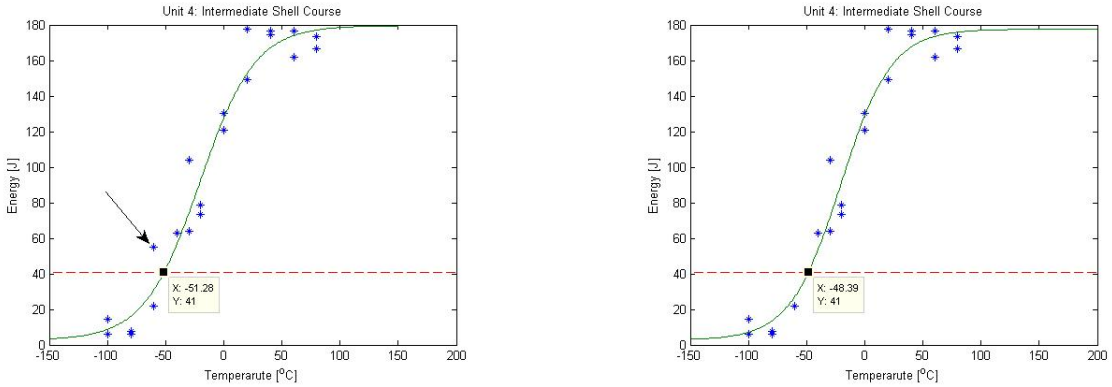

(a) All data points included.

(b) The most deviating data point removed.

Figure 10: Unirradiated ductile/brittle curve for R4, intermediate shell course.

The difference in calculated transition temperature, T_{41J}, is 2.9^oC. Assuming that this value is representative also for the calculated tanh-fits of irradiated materials, it may be compared with the variation among the considered models at specific fluence levels. Actually, a corrupt data point should have less influence on the determination T_{41J} for higher degrees of irradiation since the "steepness" of curves tend to decrease with fluence, but it still serves as an indicator of what order the error due to a corrupt data point will be. Naturally this value can grow significantly if more than one data point is faulty. I.e. if the calculated T_{41J} in a subsequent irradiated curve is shifted by an equal amount in the opposite direction, due to measurement errors, the accumulated error in ΔT will be almost 6^oC. Or, as in the considered unirradiated curve, if the two most deviating points are removed, the difference in calculated T_{41J} is just over 6^oC. In such a case, the sum of purely additive errors between two curves would be 12^oC.

As will be seen later in the comparison of models is that there is a variation between models, considering a specific material and fluence level. This is only natural since the models are not identical. However, should this variation be less than a possible error in the transition temperatures, the whole comparison may be useless.

Ringhals 4 base materials have been tested at fluence levels of 3.61 and $6.91 \cdot 10^{19} n/cm^2$. At the former fluence level the model-predicted ΔT's vary from 0.23 - 31^oC, with a standard deviation of 10^oC, in between models. Corresponding values at the higher

fluence level (6.91) are $2 - 52^oC$ with a standard deviation of 17^oC, among considered models. Here, the Ringhals 4 intermediate shell course-specific material composition has been used, see table 3.

The value 2.9 is larger than the smallest variation between models at both fluence levels. The conclusion is thus drawn that an error in testing, i.e. a corrupt data point, can be of importance when comparing models, especially at lower fluence levels. No single model can therefore be exclaimed to be superior to all others. The following model comparing analysis should rather be used to reveal certain trends for the data in comparison to models.

Furthermore, as previously stated, the determination of the accumulated flux (fluence) at the capsule positions is not a trivial matter. Since all predictive formulas aim to correlate ΔT to ϕ, an error in the latter will naturally affect the prediction of the former. Also, impact testing specimens are radially located in two layers within each capsule in Ringhals unit 3 and 4. Hence, although all specimens will be indexed with the same fluence level, the specimens located closer to the core will be subjected to a slightly higher fluence than those located in the outer layer. Naturally, this complicates the computation of transition temperatures. These subjects will not be explicitly treated in this report, but are still be mentioned as a possible sources of errors to predictive models.

4.2 Comparison Between Models

The different guides and models for prediction of the temperature shift were presented in the theoretical section above. Table 2 summarizing the considered models is repeated here as a reminder.

Table 6: Summary of models to be considered. Chemical elements of importance to the model and the fluence dependence is presented.

Model	Chemical dependence	Fluence dependence
Regulatory Guide 1.99 Revision 1	P, Cu	$\phi^{0.5}$
Reg.G.Rev.2	Cu, Ni	$\phi^{0.28-0.1\log\phi}$
FIM	P, Cu, Ni	$\phi^{0.35}$
FIS	P, Cu, Ni	$\phi^{0.35}$
Miannay	P, Cu, Ni	$\phi^{0.7}$
KTA 3203	none	ϕ^{1}
JEPE	P, Cu, Ni	$\phi^{0.29-0.04\log\phi}$
PNAE	P, Cu	$\phi^{1/3}$
E 900-02 (Reg.G.Rev.3)	Cu, Ni	$\phi^{0.5076}$ and $\tanh(\log\phi)$
EONY	P, Mn, Cu, Ni	$\phi^{0.5}$ and $\tanh(\log\phi)$

Figure 11 shows some predicted curves as determined with proper material parameters, as functions of the fluence, for intermediate- and lower shell courses in Ringhals units 3 and 4.

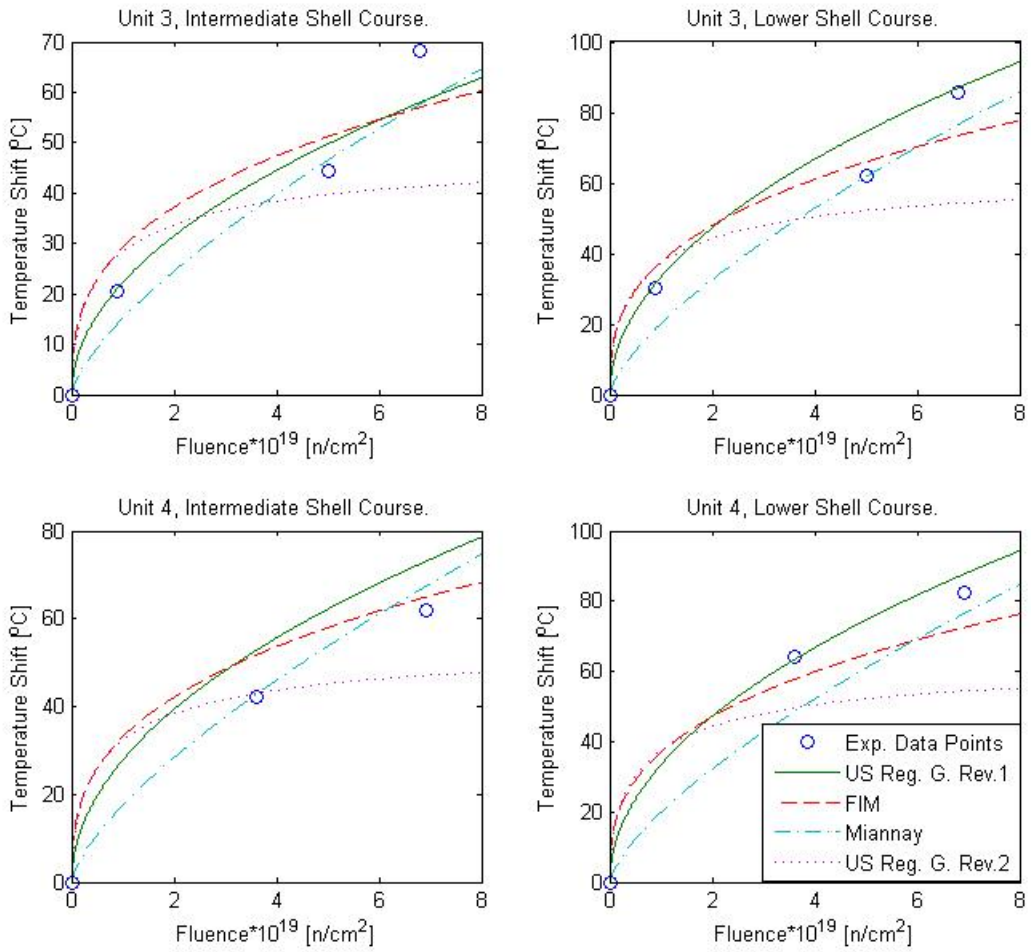

Figure 11: Experimental data and model predicted curves for all four shell courses. Only the three models with lowest errors to the measured data points, along with the current standard: US Reg. G. Rev.2, are included.

Here, due to the large amount of models, only the three best models (as will be defined and calculated below) are shown, namely Reg.G.Rev.1, FIM and Miannay along with US Regulatory Guide 1.99 Revision 2. Since the latter serves as the current model employed for transition temperature evaluation, it is included for comparison to the other models. Clearly, the model is not strictly conservative compared to measured ΔT's, especially at higher fluence levels. In fact, only two data points lie significantly beneath Reg.G.Rev.2, as seen in figure 11.

Figures showing all models and shell courses can be seen in appendix A. Some general conclusions drawn from these figures is that KTA 3203 and FIS are strictly conservative, as expected, and that the models with a larger slope at higher fluences better represent the data here (i.e. Reg.G.Rev.1, FIM and Miannay have higher exponents than all other models). Squared residual sums, S, determined in the same manner as in eq. (14), between experimental and predicted results are calculated and presented in table 7. Since the amount of data differs between units 3 and 4 (2 and 3 points, respectively), the norm of S must be used for comparison rather than S itself, i.e. S divided by the amount of

data points. KTA 3203 and FIS models are excluded since these are strictly conservative

Table 7: Norm of squared residuals.

S/amount of data	R3, Int.	R3, Low	R4, Int	R4, Low	$\sum_{allcourses} S$
Reg.G.Rev.1	45	52	120	15	560
Reg.G.Rev.2	262	374	110	496	3119
FIM	75	67	51	69	664
FIS	-	-	-	-	-
Miannay	55	77	15	142	708
KTA 3203	-	-	-	-	-
JEPE	163	270	46	383	2154
PNAE	168	474	85	712	3520
E 900-02	68	111	156	336	1522
EONY	140	235	26	334	1844
Mean	122	208	76	311	-

and are of no interest for the ΔT prediction. The last column shows the sum of squared residuals from a total of ten data points, representing all fluence levels and materials (i.e. $\sum_{allcourses,points} r_i^2$). From this set of data it is apparent that the Reg. Guide 1.99 Rev.1, FIM and Miannay formulas best represent the measured data. These are the three models with the highest fluence exponent, and they are also comparable in terms of chemical content dependance. This serves as an indication that Ringhals unit 3 and 4 RPV steels have a relatively high-exponent dependance on fluence, compared to the majority of formulas.

Furthermore, it is worth noting, in that last row, that the prediction error is higher for the lower- than the intermediate shell courses.

Another interesting observation is regarding the effect of the different chemical contents on the predictive formulas. Again focusing on the three best models, it is found that they display the largest shift for the lower shell course of unit 3 and the lowest for the intermediate shell course in unit 3. This is understandable since the R3 lower shell course is the one, among the four materials considered, that has the highest contents in Cu and Ni, while the lowest contents of the same are found in R3 intermediate shell course, as seen in table 3. Since ΔT in Rev.G.Rev.1, FIM and Miannay are all positively proportional to Cu (and Ni, to which the two latter are also proportional) they naturally display the largest and smallest temperature shift predictions for R3 lower- and intermediate shell course, respectively.

The three considered formulas are also proportional to P, but since there is no variation in this parameter its effect is neglected. Figure 12 illustrates the highest/lowest temperature shift predictions of these three formulas, along with the experimental data points from all four base metals.

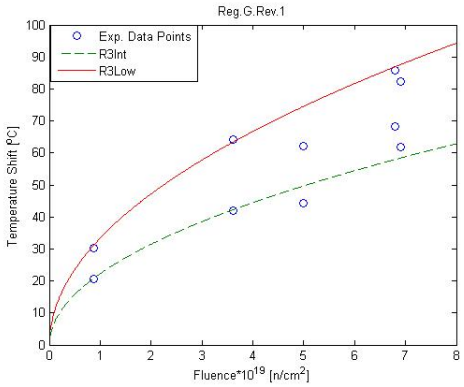

(a) US Regulatory Guide Revision 1.

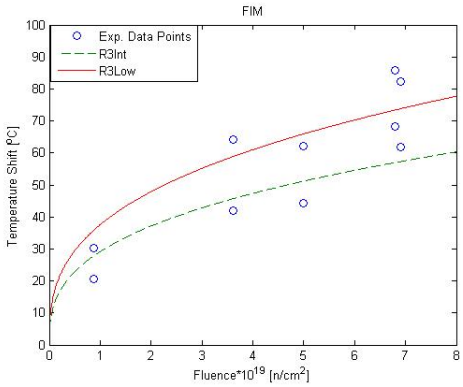

(b) FIM.

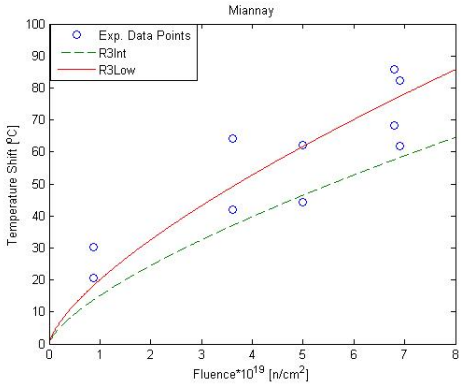

(c) Miannay.

Figure 12: Highest/lowest ΔT predictions of the three best models. All measured base metal data points are included.

For Reg.G.Rev.1 the data points are seen to lie on or between the two curves, for all points but one. This means that the variation in model predictions between the different materials is comparable to the variation among data points. For FIM and Miannay the corresponding model variation is less than the variation in measured data. In fact, as seen in figure 11, of all data points only one is underestimated using Reg.G.Rev.1, i.e. the one with highest fluence in R3 intermediate shell course. By comparing the Cu-coefficients in Reg.G.Rev.1 (556) to those in FIM and Miannay (238 and 225, respectively) it is clear that the former model is more sensitive to Cu composition than the two latter. Since the spread in Ringhals transition temperatures is comparable to the variation in Reg.G.Rev.1, among considered materials, it serves as an indication that Ringhals materials are quite sensitive to the copper composition.

Focusing on the three models with lowest errors, one may study residuals for data points versus specific parameters, as to investigate correlations between these. Residuals have been plotted and linearly fitted against element contents, for each element in table 3, so as to investigate possible residual dependencies on elemental contents. For Reg.G.Rev.1 the error, i.e. $Measured - Model$, is seen to increase linearly with Mn wt% within 95% confidence bounds, see figure 13(a). For the FIM formula no such trends exist, while for the Miannay model, the error is seen to decrease linearly with Si wt% within a 95% confidence interval, see figure 13(b). In practice, this means that introduction of a (positive) Mn term in the former model, and a (negative) Si term in the latter formula,

along with the alteration of the constant, will improve the models. Regarding the second case, a negative Si-term suggests decreasing embrittlement with increasing Si contents. Such effects are unlikely, and only the former result is taken to be potentially meaningful.

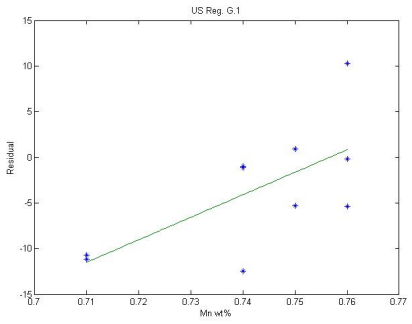

(a) Residuals for the Reg.G.1 formula versus Mn wt%.

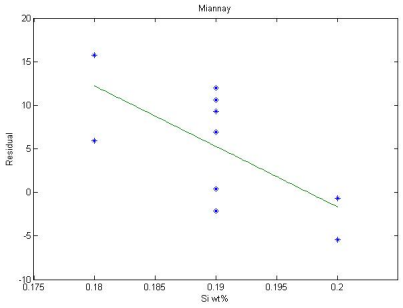

(b) Residuals for the Miannay formula versus Si wt%.

Figure 13: Of all materials analyzed only these two residual trends are clear, considering the three best models.

4.3 Influence of chemical elements

In order to analyze the effects of the different alloying elements and impurities present in the studied materials, a number of assumptions will have to be made:

1. Firstly, as will be shown, the only apparent elemental trend when comparing table 3 and figure 9 is that of Cu, considering only the base metal. Furthermore has the effect of Cu been thoroughly studied and its effect on ΔT is generally proposed to be of a linear nature. Other elements such as Ni and P are neglected since either their variation among elements is too low or their contents below suggested thresholds. The observed transition temperature shifts will thus initially be claimed to be dependant only on the Cu contents and fluence. Dependencies on these two variables are determined by minimizing residuals of an empirical model linear in Cu with varying fluence exponent. Hereby, the fluence exponent and Cu coefficient are determined. These parameters will remain fixed throughout the remaining analysis. Regarding the fluence exponent, it will be assumed to be a constant less than one. This is justified by the preceding model comparison analysis and the lack of a clear saturation effect at high fluences in the measured data.

2. Secondly, possible effects of all other elements are investigated by adding linear terms of respective element to the aforementioned formula. Again, the elemental terms will tuned so that model-data residuals are minimized.

3. From the results in step 2 no obvious conclusions can be drawn. The database is expanded with measured transition temperature shifts from Ringhals 3 and 4 weld metals, which significantly differ in chemical composition from the base metals. Here it is assumed that the same dependencies on Cu and fluence, as determined in step 1, apply also to the weld metals and that the differences in observed temperature shifts are only due to the differences in material composition. Again, elemental

effects are studied by adding terms to an empirical model and minimizing the sum of squared residuals.

4. Elemental terms studied are only either simple linear of type X or simple synergistic of type $X \cdot Y$. This is done to analyze possible transition temperature dependencies on either individual elemental concentrations, or the combined effect of two elemental concentrations. In the semi-empirical models earlier presented elemental terms are not always this simple, e.g. $\Delta T \sim Ni^2Cu$ as in FIM and FIS, or $\Delta T \sim Cu^{0.577}$ as in EONY. It is clear that the number of possible elemental combinations and elemental-exponent dependencies in elements from table 3 is infinite. Considering that the database is quite small, particular power-dependencies, such as those mentioned above, cannot be derived with statistical significance, and only these simple elemental terms are therefore analyzed.

4.3.1 Copper

An effect of Cu is, as already mentioned, clear in figure 9. No behavior on any other element is apparent by comparing figure 9 and table 3, however a combination of elemental effects or synergistic effects proposed in the different models are not as easily identified.

Also, regarding the lower- and intermediate shell course data points in figure 9 as two separate data sets, one could argue for the occurrence of "late blooming phases" for both sets. That is, a sudden increase in ΔT beyond an apparent saturation condition. Such behavior has been suggested in [6], for example, due to nucleation of Ni or MnNi phases at relatively high fluence levels.

Assuming a fit $\Delta T = (C_1 \cdot Cu + C_2)\phi^x$ represents the temperature shift behavior well, where C_1 and C_2 are constants, best-fit parameters are found by the method of sum of squared residuals, (14). These are determined to $C_1 = 418$, $C_2 = -12$ and $x = 0.52$. C_1 and x are seen to be comparable to corresponding parameters especially in the Regulatory Guide 1.99 Rev. 1, but also to parameters in the FIM and Miannay formula. The constants, however, will need to be altered with the introduction of a possible Cu-threshold, as in the semi-empirical models. It has in the above procedure been assumed that the effect of all chemical elements but Cu can be neglected, either due to too low concentrations, or too little variation in respective element.

Further assurance of a linear Cu dependence is found when eliminating the effect of fluence from the temperature shift. I.e., by previous results:

$$\Delta T(\phi) \approx \phi^{0.52}\Delta T, \tag{16}$$

so weighting the data points by $\frac{1}{\phi^{0.52}}$ should eliminate the effect of fluence. Performing this calculation and investigating ΔT(chemical element wt%) for each chemical element from table 3 shows a simple, linearly increasing behavior, within 95% confidence bounds, only for Cu, figure 14(a). For all other elements the sum of squared residuals are considerably higher than for Cu, using a linear fit. P, Ni and Mn are other elements of interest for the temperature shift. For the two former elements the wt%'s differ too little (constant for P and two different values for Ni, see table 3) in between the courses here studied, to be able to make a meaningful analysis. For Mn, on the other hand, ΔT seems to be increasing with Mn for all but the highest wt%, see figure 14(b). The same analysis has been performed for all chemical elements in table 3, and corresponding figures can be found in appendix B.1.1.

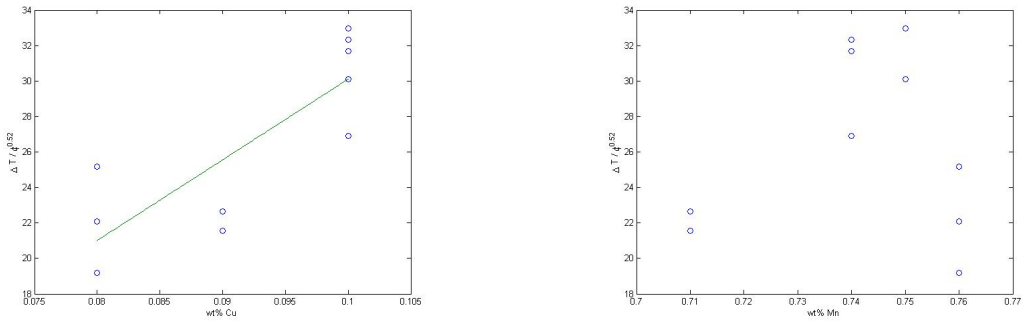

(a) Effect of Cu on $\Delta T/\phi^{0.52}$.

(b) Effect of Mn on $\Delta T/\phi^{0.52}$.

Figure 14: Effect of chemical wt%'s on $\Delta T/\phi^{0.52}$.

In the analysis of residuals between Reg.G.Rev.1 and data, Mn was identified to be correlated to the error. Due to the correspondence between C_1 and x and parameters in aforementioned formula, it is reasonable to expect some dependence on Mn.

Although Cu thresholds are generally set to $\sim 0.08wt\%$, this is by no means universally true. Observing figure 14(a), one notices that between the two lower Cu concentrations the average increase of $\Delta T/\phi^{0.52}$ is negligible. Hence, a possible threshold may lie beyond this range, but before $Cu = 0.1$ where the increment is more noticeable, i.e. $0.09 \lesssim Cu_{threshold} < 0.1$. Naturally, these are just speculations, since three discrete values of Cu wt%'s hardly suffice for a detailed analysis. This may however also explain why the final three points (the three data points with the highest Mn contents) in figure 14(b) deviate from a supposedly linearly increasing Mn-pattern. These three points are namely those of the R3 intermediate shell course, which is the material with the lowest wt% in Cu (0.08 wt%). If a Cu threshold, slightly above 0.08 wt%, exists than this may be the cause of the lower ΔT's for this material, since the effect of Cu should disappear here.

4.3.2 Additional elemental dependencies

Possible dependencies on other elements are studied by introducing linear elemental terms X to the above determined Cu, ϕ relationship:

$$\Delta T = (418Cu + \alpha X + const)\phi^{0.52}, \tag{17}$$

Equation (17) is optimized by tuning α and *const* so that the sum of squared residuals is minimized. This has been performed for all elements, and the results are shown in table 8. Of all elements, it seems that $X = Mn$ gives the best predictions in terms of a formula

Table 8: Residuals of empirical models (19), linear in Cu and element X. α and *const* are fitted by the least squares method to base metal data.

Element X	C	Si	Mn	P	S	Cr	Mo	Ni	V	Co	Al	Cu
Sum of squared residuals	332	253	219	373	373	276	332	373	373	344	354	373
Error % compared to $X = Mn$	51	15	0	70	70	26	51	70	70	57	61	70

(17). However, in the above comparison, Mn is far from superior compared to all other materials, and it is obvious that no conclusion can yet be drawn.

In order to continue the analysis, primarily to study the effect of Ni and Mn, the database needs to be extended, and the results for Ringhals 3 and 4 weld metal is included. For the weld metals the wt%'s of Ni and Mn are considerably higher, while for Cu they are comparatively low [9], as seen in table 3. The Charpy test results are taken from [9], and given in tables 9 and 10.

Table 9: Ringhals Unit 3, Weld Metal

Fluence$\cdot 10^{19}$ $[n/cm^2]$ $(E > 1MeV)$	0	0.88	5	6.79	6.79
T_{41J} $[^oC]$	-69	-3	118	161	184
ΔT_{41J} $[^oC]$	0	66	187	230	253
USE $[J]$	193	166	131	118	98
ΔUSE $[J]$	0	-27	-62	-75	-95

Table 10: Ringhals Unit 4, Weld Metal

Fluence$\cdot 10^{19}$ $[n/cm^2]$ $(E > 1MeV)$	0	3.61	6.05	6.91
T_{41J} $[^oC]$	-97	28	58	87
ΔT_{41J} $[^oC]$	0	125	155	184
USE $[J]$	175	144	119	107
ΔUSE $[J]$	0	-31	-56	-68

It should be noted that there is a difference of 23^oC in ΔT between the two last columns of table 9, even though the fluence and material composition is identical. This value serves as measure of what the size of the error in ΔT might be. Naturally, the magnitude of errors are the sum of many uncertainties, not only in the calculation of ΔT.

For the weld metal the ΔT vs. ϕ increment is larger than for the base metal. This discrepancy compared to the base metal is attributed to the effect of having a different chemical composition. Naturally, weld metals should respond differently to embrittlement compared to base metals, due to the difference in fabrication, and ultimately, also structure, but it shall here be assumed that their only difference is the chemical composition. In other words, the same fluence behavior will be employed for the weld metals. Also, the Cu dependence, as derived for the base metal, will be assumed to apply also for weld materials. This is done since Cu contents are lower in the weld metal. Any attempt to optimize Cu coefficients to the data will thus give a negative Cu dependance, clearly contradictory to all theory.

As proposed in many of the models, ΔT should increase linearly with P. If this was the case, Ringhals 4 should display a larger shift due to its higher content of P, but here the opposite is true. No correlations with P are found in the data considered. Contents of P are however low, and the spread among data points is small, for all materials here studied, and the effect of P will in this study be neglected.

It is proposed in [14], among others, that Mn in combination with Ni can be of importance when the contents are sufficiently large. This is indeed the case for Ringhals 3 and 4 weld metals. Figure 15 shows the weighted $\Delta T/\phi^{0.52}$ data points along with their Mn, Ni concentrations.

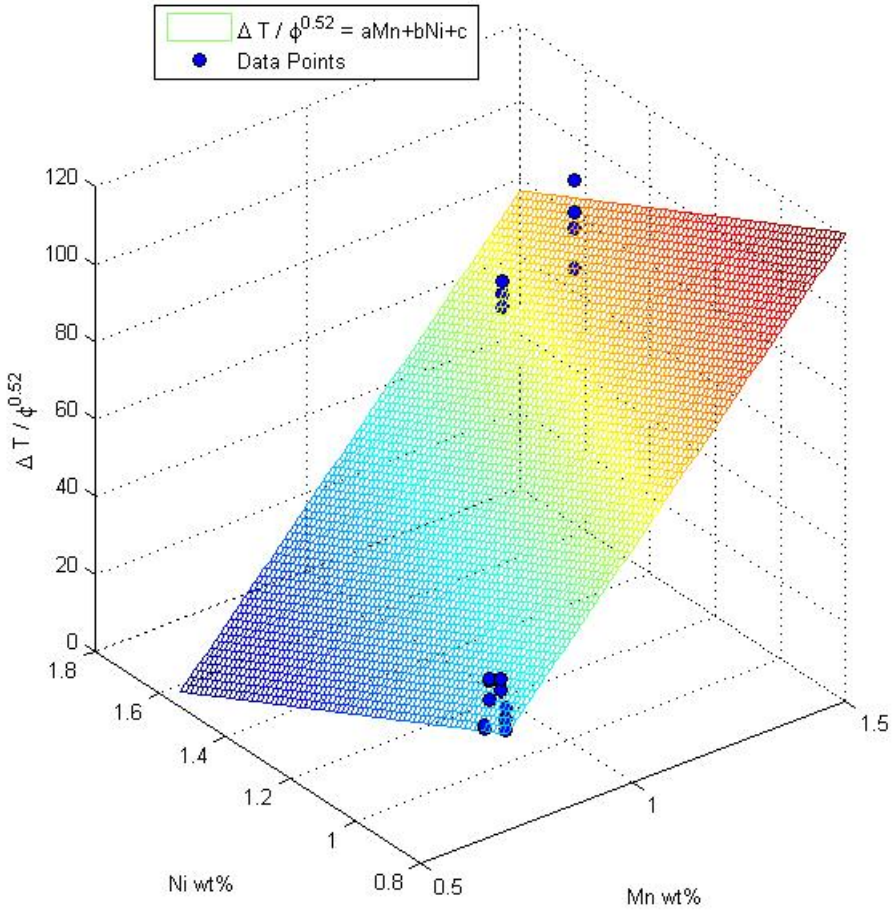

Figure 15: Effect of Mn and Ni on $\Delta T/\phi^{0.52}$.

Included is a linear polynomial fit, of type $aMn + bNi + c$, displayed as a surface. Exactly what dependence on Mn, Ni applies is hard to determine, but it is clear that the temperature shift is greatly increased for higher contents of these elements. The surface fit predicts an increasing behavior for Mn ($a > 0$), while, somewhat surprisingly, a slowly decreasing behavior with increasing Ni contents ($b < 0$).

In [14], the temperature shift is suggested to increase linearly with both Mn and Ni contents, i.e. $\Delta T \sim (A \cdot Mn + B \cdot Ni + const) f(\phi)$, where $f(\phi)$ models the behavior due to fluence. Additionally, it is reasonable to assume that a synergistic effect between Mn, Ni might exist [6]. This will be supplied here in the simplest case of $C \cdot MnNi$. Assuming that an exponent of 0.52 correctly explains the behavior of ΔT on fluence also for the weld metal, and that the Cu-behavior derived for the base metals applies also for the weld metals, an initial attempt to optimize the following formula to base- and weld metal data is performed:

$$\Delta T = (418Cu + AMn + BNi + CMnNi + const)\, \phi^{0.52}. \tag{18}$$

Constants A, B, C and *const* are optimized to fit the data, again by the sum of squared residuals technique in (14). These are determined to $A = 110$, $B = 19.6$, $C = -16.8$

and $const = -100$, giving the result shown in figure 16. Values of the coefficients suggest that ΔT increases with Mn and Ni concentrations, but decreases with the synergistic MnNi effect. However, A is larger than B and C, by more than a factor of five. In other words, the effects of Ni and MnNi are almost negligible in comparison to Mn. In figure 15 the surface fit suggested a negative (small) Ni-coefficient. In the above analysis the corresponding Ni-coefficient was determined to be positive (small). The reason for this discrepancy is that the algorithm used in the MATLAB fitting function, used for calculating the surface fit, is slightly different from that employed here. Also, no MnNi term was included in the surface fit, which may effect the Ni-coefficient. The fact that the calculated Ni-dependence is determined to be quite different by the two different methods (and consistently small compared to the effect of Mn) serves as another indication that the ΔT/Ni correlation is weak in the data available. The predicted results agree well

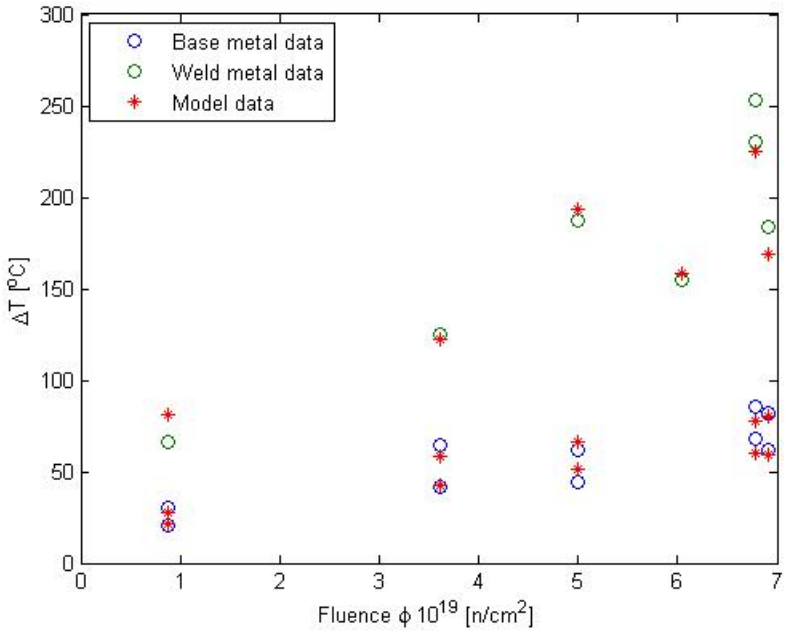

Figure 16: Data points for base- and weld metal along with the predicted results from eq. (18). The model-predicted results are seen to agree well with experimental data points for both base- and weld metals.

with the test results for both base- and weld metals. It needs to be said, however, that no thresholds whatsoever have been considered in the above procedure. In other words, the effect of Cu, Mn and Ni are included also in materials with low content of respective element. Also, no distinction has been made between weld- and base metals (except for the chemical contents). In several of the models explained above, such a distinction exists. Nevertheless, this simple model, linear in Cu, Mn, Ni and MnNi, with a fluence exponent of 0.52, still gives a reasonable explanation of the transition temperature shift for these particular materials. Even considering only base metal data, the squared residual error is improved by ∼40%, compared to the model including only the Cu effect.

In fact, Ni and MnNi need not even be included in this model, as will be seen.

The effect of the remaining chemical elements are studied in the same manner. Addi-

tional simple models have been considered

$$\begin{aligned} \Delta T &= (418Cu + \alpha X + const)\phi^{0.52} \text{ or} \\ \Delta T &= (418Cu + \alpha X \cdot Y + \beta Z + const)\phi^{0.52}, \end{aligned} \tag{19}$$

where X, Y and Z are the elements considered and α, β and *const* are the parameters varied for finding the best fit). It is found that including Ni and MnNi to the model in (18) in fact only very slightly improves the situation (the squared residual error is reduced by less than one percent). The results suggest that Mn has the dominant contribution to the shift. It should be noted that, although not as well as Mn, also $X = Ni$ is able to reasonably reproduce results. This is true especially for the base metal data, while mutual differences within weld metal data are predicted with a lesser amount of success.

As seen in table 11, apart from Mn and Ni, also C and to some extent Cr, are able to reproduce results reasonably. They do, however, fail in predicting the mutual shift relations for either the base material or weld material, whereas (19) with $X = Mn$ displays a good agreement with measurements from both weld and base metal. C and Cr both have a negative proportionality constant ($\alpha < 0$), suggesting that the shift decreases with increasing concentration. This means that increasing concentrations of these two materials should counteract the embrittlement. Although desirable, no such elemental effects have been recorded in literature. It will henceforth be assumed that these are not "real" effects, rather the ability of C and Cr to reproduce measured data is due to the difference in respective elemental contents between the base- and weld materials. Studying table 3 it is clear that contents of both of these elements are lower in the weld- than the base material.

Thirdly, after Mn and Ni, also Al is able to represent results reasonably. Again, levels of this element are larger in weld materials than in base materials. Embrittlement is generally not accredited to the presence of Al in literature, but here it will be mentioned as an unlikely but possible candidate. Results for all elements, X or $X \cdot Y$ and Z, are plotted and shown in appendix B.1.2.

Table 11 shows the sum of squared residuals between all fitted models, with element X or $X \cdot Y$ and Z, and measured data points. Comparing models "MnNi" and "MnNi,Ni",

Table 11: Residuals of empirical models (19), linear in Cu and element X, or linear in Cu, $X \cdot Y$ and Z. Coefficients are fitted by least squares method.

Element X	C	Si	Mn	P	S	Cr	Mo	Ni	V	Co	Al	Cu
Sum of squared residuals (10^4)	0.24	8.00	0.11	3.55	5.28	0.32	2.06	0.38	0.63	8.18	0.50	4.50
Error % compared to $X = Mn$	115	6938	0	3026	4539	178	1709	234	454	7094	342	3859
Element $X \cdot Y$ or $X \cdot Y, Z$	MnNi, Ni		CuMn		CuNi		MnNi		CuMn, Mn		CuNi, Mn	
Sum of squared residuals (10^4)	0.17		4.44		4.34		0.17		0.11		0.11	
Error % compared to $X = Mn$	55		3940		3850		55		0		0	

the errors are seen to be identical. Actually, the Ni coefficient is calculated to be equal to

zero by the least squares method. Similarly, for all models containing an $X = Mn$ term, the coefficients of the remaining terms (i.e. CuMn and CuNi) are all equal or close to zero.

From table 11 it is clear that Mn is strongly correlated to the transition temperature shift. Any equation (19) containing an Mn term gives the lowest error to measured data. Including additional terms to an Mn term does little to improve the error, and coefficients for these terms will be calibrated to, or close to, zero. Somewhat surprisingly, no Ni- or MnNi dependencies can be identified. Usually temperature shifts are accredited to Ni rather than Mn, however to say that Ni has no effect at all in Ringhals 3 and 4 base material embrittlement would be to great an assumption. By the statement: "for a given high level of nickel in the material and all other factors being equal, high manganese content leads to much greater radiation-induced embrittlement than low manganese content for both VVER-1000 and PWR materials" from [4], one could argue that the embrittlement is due to both Ni and Mn, but only manifested through Mn. Among the base metals the variation in Mn is indeed greater than that in Ni, whereas they are comparable for the weld metals.

The effects of Ni may in fact be present but lost in the analysis due to the low amount of data points and relatively high measurement errors. Another possible explanation is that Ni contents may be below a possible threshold, while Mn contents exceed a possible threshold. For instance, thresholds suggested in [13, 21] are $Ni_{threshold} = 1.5$ wt% and $Mn_{threshold} = 0.8$ wt%. Comparing these values to those in table 3, it is clear that Mn exceeds this threshold for the weld metals while the base metals are close to the threshold. Contents of Ni, on the other hand, are below the threshold for the base metals and only marginally above it for the weld metals. Values of thresholds, as the ones given above, often differ between reports, and cannot be taken to be universally true. In fact, as suggested in [6], Mn and Ni thresholds may decrease as the Cu contents increase. These uncertainties make the analysis difficult, however, what is worth noting about the thresholds stated above is that the one for Ni is almost twice that of Mn. This means that although contents of Ni and Mn are comparable in both base- and weld-metals, effects due to Mn are more likely to be noticeable than effects due to Ni.

Additional synergistic terms; CuNi, as suggested in the FIM and Miannay models, and CuMn have been added to (19), and parameters fitted accordingly. As for the case with Ni and MnNi, these improve the residual error only very marginally, and the conclusion is that a model linear in Cu and Mn is sufficient:

$$\Delta T = (418Cu + 91Mn - 79)\,\phi^{0.52}. \tag{20}$$

Instead, when minimizing models (19), only considering the base metal data (in the analysis above that led to (20), both weld and base data was used), $X = Mn$ was found to be the parameter giving the lowest error to measured data, however advantages to other materials were not as convincing as in table 11. Coefficients α and *const* were in this case determined to 96 and -83, respectively. Compared to 91 and -79, as in (20), these values are almost identical. In practice, this means that optimizing a model linear in Cu and Mn and with a fluence exponent of 0.52 to base metal data, actually provides a model which can reasonably predict the behavior of also the weld metal. The fact that the resulting models, considering two very different data regions, are essentially the same indicates that (20) indeed contains effects common for all Ringhals materials.

Furthermore, the calculated negative $const = -79$ may be due to thresholds, not explicitly given in the model. Introducing thresholds to (20) will alter the constant, i.e. $\Delta T = (418(Cu - Cu_{threshold}) + 91(Mn - Mn_{threshold}) + const_2)\phi^{0.52}$, where $const_2$ may be equal to, or greater than zero. For example, employing thresholds of 0.08 and 0.8 wt% for Cu and Mn, respectively, gives the formula: $\Delta T = (418(Cu - 0.08) + 91(Mn - 0.8) + 27)\phi^{0.52}$. Such a model resembles the semi-empirical formulas previously defined.

A 3D representation of (20), similar to figure 15, is seen in figure 17. Again ΔT is divided by the fluence dependence $\phi^{0.52}$. Weld- and base metal data is here included, as noticed in the two distinct data point regions in the figure.

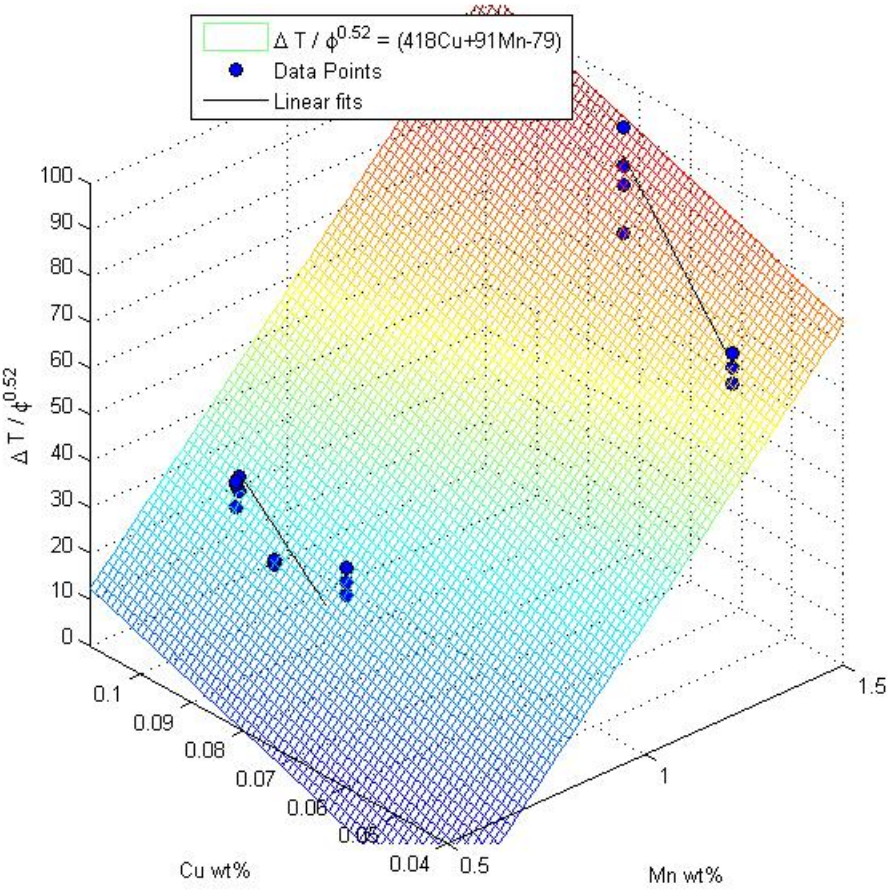

Figure 17: Data points for base- and weld metal, divided by $\phi^{0.52}$. Predicted results from (20), i.e. $\Delta T/\phi^{0.52} = 418Cu + 91Mn - 79$, are represented by the surface.

Data points in both regions fit onto the surface, given by (20), reasonably. Furthermore, equation (20) is shown in figure 18, as compared to the Reg.G.Rev.1, FIM and Miannay formulas for the base metals displaying the highest shift (lower shell courses in R3 and R4).

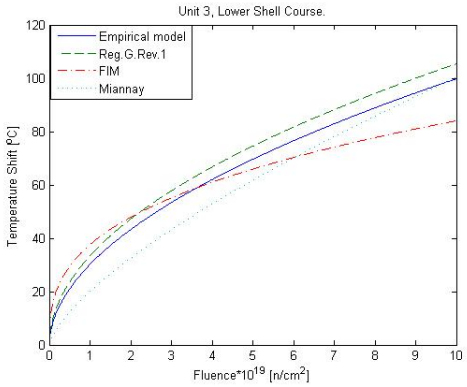

(a) R3 lower shell course.

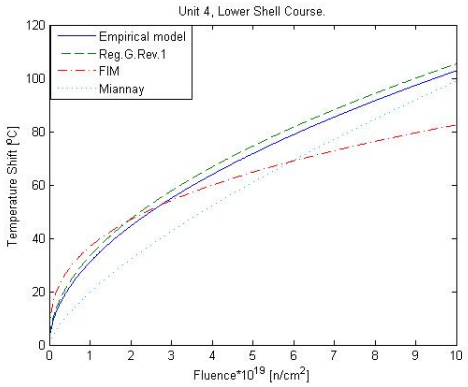

(b) R4 lower shell course.

Figure 18: The empirical model (20) compared to Reg.G.Rev.1, FIM and Miannay formulas. The fluence, ϕ, extrapolated to $10 \cdot 10^{19} n/cm^2$.

At $\phi = 10 \cdot 10^{19} n/cm^2$ (20) gives a $\Delta T = 99.8$ and 102.8^oC for the two materials. The model is seen to be comparable to Reg.G.Rev.1 for all fluences for both metals. Essentially, these two are almost identical, except for the Mn term given in the empirical model.

Additionally, the residuals between (20) and the data may be used to investigate the effects of other chemical elements. As described in the evaluation section above, if (20) is indeed a good fit to the data, then no trends should be observed between the residuals and chemical variables. If, for instance, certain data points are underestimated for high contents of a specific chemical parameter there may be some dependance on that parameter. This analysis has been implemented for all chemical elements, X, and all simple synergistic effects of type $X \cdot Y$, and no certain trends are clear. Neither strictly increasing or decreasing linear behavior of residuals versus X or $X \cdot Y$ are certain within 95% confidence bounds. See appendix B.2 for graphical presentations of these results.

The standard deviation of residuals between (20) and measured data is 8^oC, considering both weld- and base metal data, and 5^oC when considering only base metal data. These values are certainly comparable to measurement errors (e.g. 3^oC as determined by studying the effect of one corrupt data point in the determination of the transition temperature) indicating that the model is indeed a good fit to the data. The differences in model predictions from measured data are shown in figure 19 as deviations from the straight line "$y = x$".

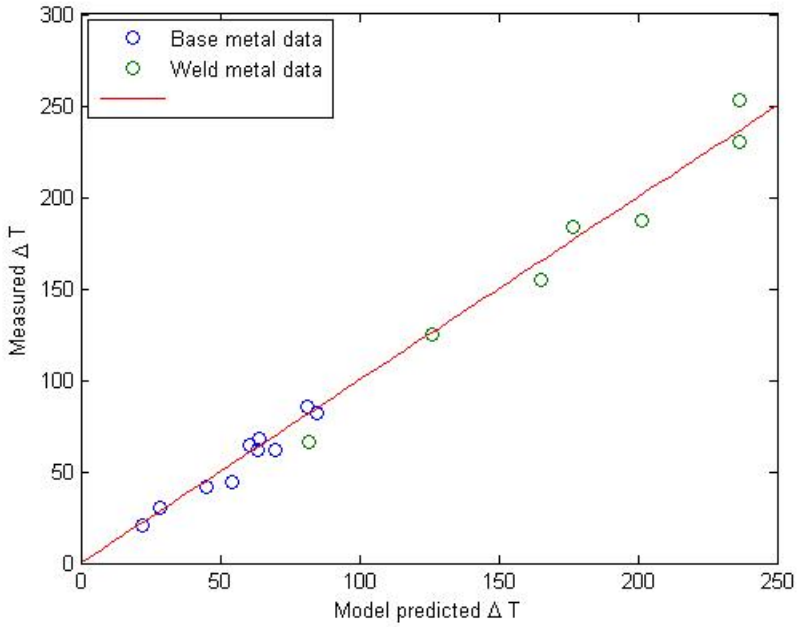

Figure 19: Model predictions vs. measured results for the transition temperature shifts. For an ideal model all points should lie on the straight line.

The empirical model (20) is an exponential function of fluence, ϕ, with an exponent less than one. It therefore exhibits a saturation behavior for increasing fluence. The previously suggested "late blooming" effect for the base metal is in contradiction with this saturation. Also for the weld metal no saturation effect is apparent. The empirical model is thus likely to underestimate ΔT at higher fluences. Consequently, as a result of the model optimization by the procedure in (14), ΔT should be overestimated at lower fluences. Studying figure 16 this seems generally true, with the exception of a few data points.

The model in (20) is not claimed to be true for predicting embrittlement in Ringhals 3 and 4 materials. Nor is the purpose of the report to develop such a formula, rather to investigate what parameters are important for predicting the observed temperature shifts. It is merely a best fit to the data available, and the performed analysis shows that correlations between materials, fluence levels and temperature shifts are greatest for the materials Mn and Cu and a comparatively high fluence exponent behavior ($\gtrsim$0.5). Additional effects, such as a suggested Ni dependance, may be lost due to the very low amount of data, or due to the potentially large errors in calculated ΔT's.

Regarding the first issue, is that there are only six different materials considered. Thus there are maximally six discrete concentrations for each element, while the amount of elemental parameters is twice as large. Any material dependencies derived from this database are therefore of poor statistical quality.

Secondly, a best fitted model $\Delta T = (418Cu + \alpha Ni + const)\phi^{0.52}$ for example, exhibits a standard deviation of residuals of $\sim$15^{o}C. As calculated, one corrupt data point can result in an error of around 3^{o}C in determination of the temperature shifts. Since ΔT is a difference between temperature shifts, and that more than one data point naturally may be corrupt, errors of $\sim$15^{o}C or more are not unlikely. For instance, in the case of the highest-fluence weld metal points in R3 (see table 9), the calculated transition temperatures differ

by 23^{o}C, although the fluences and materials are identical. Depending on the magnitude of these errors, a ΔT vs. Ni dependance may therefore be lost. A further source of errors, not explicitly treated in this report, may be in the determination of the fluence, which naturally affects the prediction of ΔT.

Although thoroughly studied and included in most semi-empirical models, no dependence on phosphorous has been identified. The threshold is generally considered to be 0.008 wt%, a value exceeded for the weld metals. These levels may however be too low still, to notice a significant effect in the transition temperature.

Also Si is occasionally included in the discussion regarding RPV embrittlement. No effects of Si have been recognized in the considered data. However, as seen in the analysis of the semi-empirical models, the temperature shift - model residuals indicated some Si dependance for the Miannay formula (figure 13(b)). In other words, the data suggests a possible Si dependance in the case of higher fluence exponent behavior (i.e. an exponent of 0.7 in the Miannay model).

4.3.3 SIMCA P+

The statistical analysis software SIMCA P+, developed by Umetrics AB, has been employed. Considering only the base metal data, the software identifies Cu as the chemical parameter most correlated to the shift. Including the weld metal to the data set, SIMCA points to Mn as the dominating chemical parameter. These results agree well with conclusions in the above sections. However, since the number of data points is relatively small, any statistical measure will be of poor quality in this sort of analysis.

4.4 PERFECT calculations

PERFECT has been used to calculate the increase in hardness due to irradiation. Although four different chemical contents may be defined in PERFECT (Cu,Si,Ni,Mn), the current version of the software only takes Cu into account for the calculation. However, for any nonzero Cu content, the program runs into difficulties, i.e. the Cu contents are not kept constant through the calculation. This problem arises during the rate theory stage of the algorithm. Although understanding and modeling at the initial cascade forming stage is well understood, difficulties arise in the long term diffusion calculations. Cascades form and annihilate within tens of picoseconds, while the operation of power plants, and hence the radiation enhanced diffusion of solutes, goes on for several tens of years. Combining these two very different timescales naturally presents tremendous difficulties, calculational and theoretical.

Currently, calculations with material parameters such as those in Ringhals 3 and 4 base materials (i.e. Cu contents 0.08-0.1 wt%) cannot be implemented in PERFECT. It is, however, possible to perform calculations for a pure material. Parameters to be defined in such a case is the neutron spectrum, flux (averaged over the total plant operation), total time of irradiation (which hence gives the fluence) and the yield strength of unirradiated materials. The results for Ringhals 3 materials are shown in figure 20.

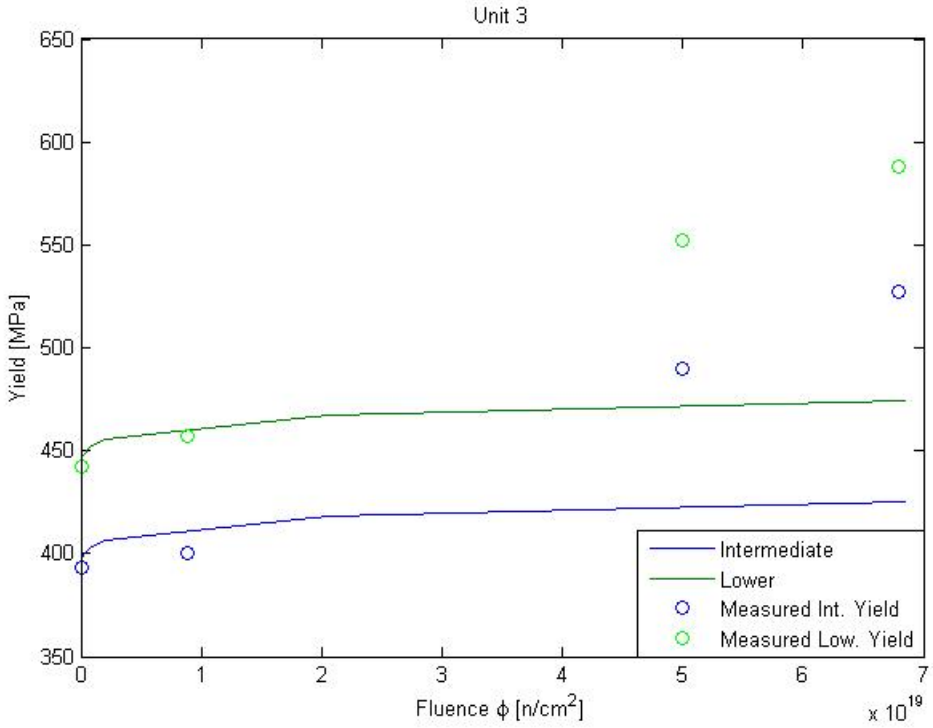

Figure 20: PERFECT calculations of yield strengths for intermediate- and lower shell course base metal. No material composition is taken into account.

Included are the measured yield strengths at fluence levels of 0, 0.88, 5 and $6.79 \cdot 10^{19} n/cm^2$, as determined by tensile testing [9]. PERFECT calculations clearly underestimate the yield strength at high fluences, by approximately 100 MPa. The same trends are visible for Ringhals unit 4.

Possibly PERFECT may be used for analysis of hardening in very pure materials, i.e. low contents in Cu. For Ringhals 3 and 4 materials however, it seems to be a superfluous tool.

4.5 Effect of fluence

By the least squares method the fluence exponent was determined to 0.52, using a model linear in Cu, considering the base metal. This is certainly comparable to the $\Delta T \sim \sqrt{\phi}$ dependence derived for low Cu steels (damage due to MF's). Since all materials here considered may be classified as low Cu steels the results agree well with theory (under the assumption of a $Cu \lesssim 0.1wt\%$ definition, however such definitions vary). The embrittlement is in such cases dominated by matrix damage rather than precipitates, i.e. nanofeatures responsible for the embrittlement are thus suggested to be MF's. Microstructural analysis might confirm this assumption.

Later it was assumed that the same exponent might be used to explain also the weld metal data, along with the introduction of a Mn term. Actually, optimizing a model: $\Delta T = (aCu + bMn + const)\phi^x$, to base- and weld metal data gives an exponent, x, closer to 0.6. The assumption that the weld- and base should have the same fluence behavior is rather grave. It is however clear that all materials have a relatively high-exponent

dependance on the fluence, and that it is close to or above 0.5. No strong saturation behavior, as predicted in Reg.G.Rev.2 or JEPE formulas for example (by introduction of a $\log \phi$ term in the exponent), can be seen at high fluence.

4.6 Effect of flux

In order to study a possible dependance on the fluence rate/flux the Ringhals 2 surveillance results are included. The reason for this is that whereas the angular positions of surveillance capsules in R3 and R4 vary by only 3^o, the positions of capsules removed from R2 vary by 10^o. Correspondingly, there will be a larger variation in the flux. Figure 21 shows the radial and angular fluence distributions in the R2 RPV after 32 cycles, calculated using multigroup transport theory.

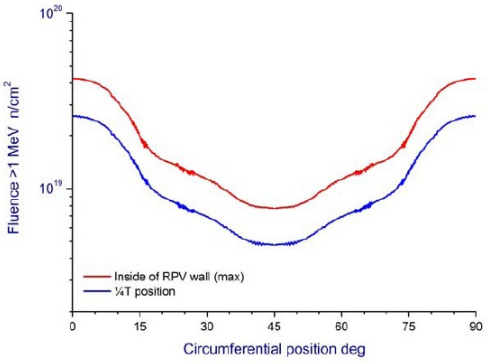

(a) Angular fluence distribution.

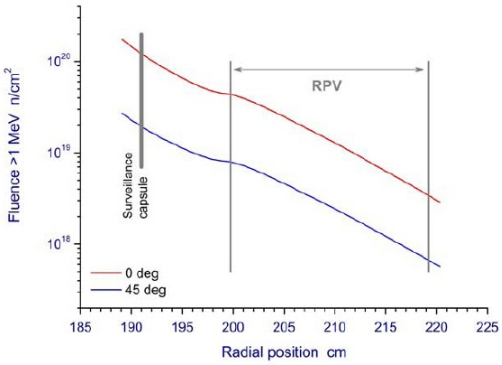

(b) Radial fluence distribution.

Figure 21: Fluence distribution for Ringhals 2, calculated at 32 cycles, [25].

32 cycles correspond to 23.5 effective full power years (EFPY), or $23.5 \cdot 365 \cdot 24 \cdot 60 \cdot 60$ s. By dividing with this number figure 21(a) is hence translated to the (operation - averaged) flux. This is not really of importance since we only wish to compare fluxes at the positions of the removed capsules, namely at 15^o and 25^o. The ratio of fluxes at these positions is naturally the same as the ratio of fluences after 32 cycles at the same positions. Also, as seen in figure 21(b), the fluence (and flux) varies approximately identically regardless of angular position between capsule positions and the inner RPV wall. The ratio of average

fluxes at capsule positions is thus equal to the ratio of fluxes at the inner RPV wall. Hence, the data points of interest are given in the blue curve of figure 21(a) at 15^o and 25^o. Specifically, capsules located at the former position experience a larger average flux, roughly by a factor 2, than those located at 25^o.

The Ringhals 2 surveillance programme includes only the lower shell course for the base metal. These specimen comprise axially and tangentially cut samples. This means that they were cut out of the shell course in a direction either parallel or perpendicular to the length of the circular shell course, in order to investigate an embrittlement dependance on this directional parameter. Such an effect is not clear, and axial and tangential base metal will be studied separately.

The base metal transition temperatures, taken from [25], are shown in table 12.

Table 12: Ringhals Unit 2, Temperature Shifts

	Tangential				
Fluence$\cdot 10^{19}$ $[n/cm^2]$ $(E > 1MeV)$	0	0.42	1.36	2.59	6.01
Angular position	-	15^o	25^o	25^o	15^o
T_{41J} $[^oC]$	-50	-10	-11	-2	26
ΔT_{41J} $[^oC]$	0	40	39	48	76
	Axial				
Fluence$\cdot 10^{19}$ $[n/cm^2]$ $(E > 1MeV)$	0	0.42	1.36	2.59	6.01
Angular position	-	15^o	25^o	25^o	15^o
T_{41J} $[^oC]$	-8	11	17	22	50
ΔT_{41J} $[^oC]$	0	19	25	30	58
	Weld				
Fluence$\cdot 10^{19}$ $[n/cm^2]$ $(E > 1MeV)$	0	0.42	1.36	2.59	6.01
Angular position	-	15^o	25^o	25^o	15^o
T_{41J} $[^oC]$	-51	-30	-18	-26	5
ΔT_{41J} $[^oC]$	0	21	33	25	56

Figure 22 shows the temperature shifts for R2 base material (tangential and axial) and weld material. Also included is the US Reg. Guide 1.99 Rev.2, with appropriate chemical factors (recall equation (2) and the corresponding discussion).

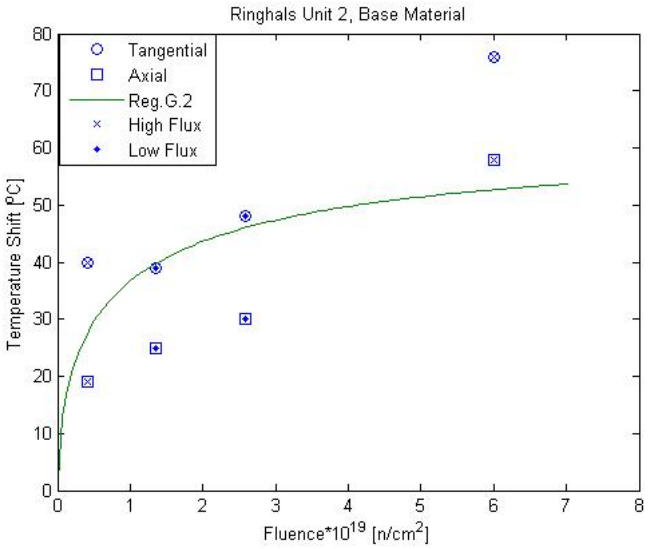

(a) Base material, tangential and axial.

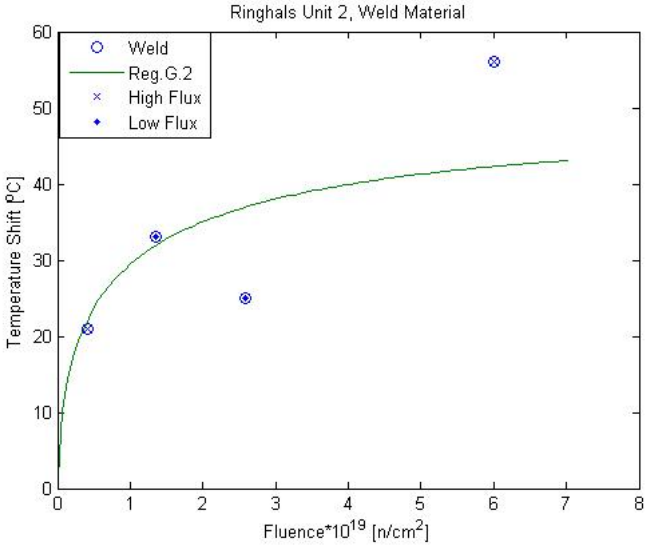

(b) Weld material.

Figure 22: Ringhals unit 2 base and weld material, along with US Reg.G.2.

Studying the tangential and axial data points (circles and squares, respectively) in figure 22(a) separately, it is clear that the high-flux data points display higher temperature shifts than the low-flux data points in respective material. I.e. for the tangential material the high-flux points are underestimated, while the low-flux data agree well with the model. In the axial material high-flux points are close to the model while low-flux points are overestimated.

Studying the weld metal in figure 22(b), the same trend is observed. The high-flux data points are either close to or above the Reg.G.Rev.2 prediction, while the low-flux points are either close to or below the model. Figure 23 illustrates the same conclusion. The majority of high-flux data points are seen to be under predicted compared to the model, while the opposite is true for the low-flux data.

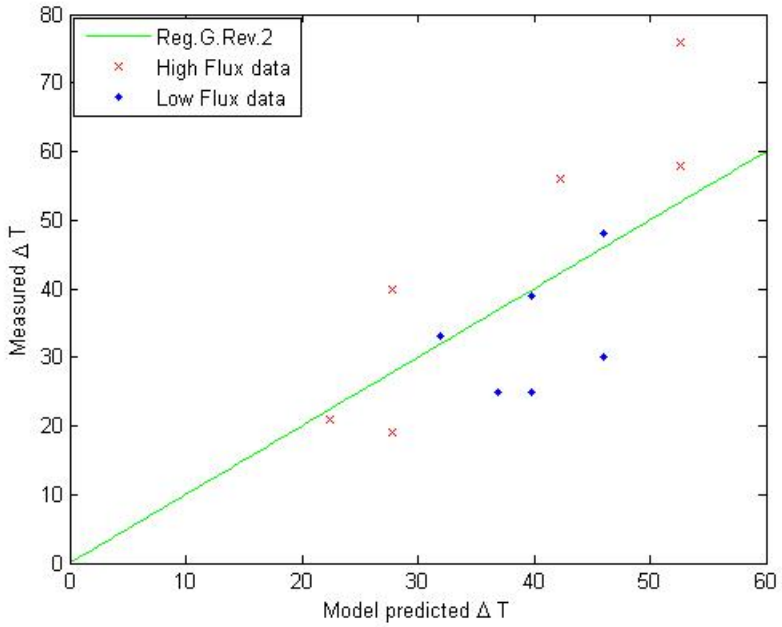

Figure 23: Measured transition temperature shifts, vs. Reg.G.Rev.2 predictions. All Ringhals 2 materials are included, i.e. tangential/axial base metal data and weld metal data.

By the analysis above it is clear that the effect of doubling the flux exposure is noticeable in terms of the transition temperature shift for Ringhals 2 specimens. Naturally, no explicit behavior of ΔT on flux can be derived from a mere two discrete flux levels. However, an increase of ΔT with flux is consistent with all Ringhals 2 materials.

4.7 Conclusions

The temperature shifts have been calculated for all shell courses in reactors 3 and 4 and are seen in figure 9. The models are evaluated relative to these results. The KTA 3203 and FIS models are found to be strictly conservative for all data points.

Among the considered models the ones in best agreement with the experimental data are the Reg. Guide 1.99 Rev.1, FIM and Miannay formulas. This was determined by comparing the norm of squared residuals for all models, see table 7. These formulas are similar in that they are all linear in Cu, with proportionality constants ranging from ∼225-555, and in P, which has been neglected since its composition doesn't vary in between materials, and that they all exhibit a relatively high-exponent fluence dependance. Also, in the two latter models some Ni- and CuNi-synergistic effects are included.

Generally the embrittlement, and the temperature shift, is expected to saturate at high fluence levels, as is the case in all models but KTA 3203. The base metal results seem to saturate in the region $3.5\text{-}5{\cdot}10^{19}$ n/cm^2, but increase again at higher fluences. Such behavior, which may be due to "late blooming", has been identified and discussed in several reports (e.g. [4, 6, 14]).

The dependance on material composition has been investigated. It is seen that the temperature shifts increase with increasing Cu contents in the base metals. Under the

assumption that the shift is linear in Cu, the proportionality constant and fluence exponent is determined to 418 and 0.52, respectively, by the least squares method. No other dependance on any chemical element is apparent, and the weld metal data is added to the analysis. Attributing the deviation in temperature shifts solely to the difference in chemical compositions it is shown that shifts should increase with increasing Mn contents, while Ni and MnNi synergistic effects are negligible. Also considering only the base metal, the same Mn dependance can be derived. No dependance on other elements or Cu-synergistic effects have been identified. Nor are any trends between model (20) residuals and elemental composition or synergistic effects clear. It is seen that both base- and weld metal data points can be reasonably represented using a model linear in Cu and Mn with a fluence exponent of 0.52. Even base metal data points are better explained by the introduction of this Mn term.

The temperature shift is found to have a relatively high-exponential behavior on fluence, as seen in the comparison of semi-empirical models. The least squares method suggests an exponent of ~ 0.5 for the base metal, while the same method predicts an exponent closer to 0.6 when also the weld metal is included to the database.

Studying Charpy measurements from Ringhals 2 base- and weld metals certain conclusions regarding the effect of flux on the transition temperature shift can be drawn. Half the samples hereof are subjected to a roughly twice as large fluence rate compared to the rest. Consistently, all material samples exposed to the larger flux rate display a larger ΔT, as found comparing the data points to US Reg.G.Rev.2.

5 References

[1] IRRADIATION EMBRITTLEMENT MITIGATION, EUR 16072 EN, AMES Report No.1, Tapio Planman, Reijo Pelli and Kari Törrönen, Espoo (1994).

[2] Vattenfall Official Website, http://www.vattenfall.com/en/index.htm

[3] IAEA Second International Symposium on Nuclear Power Plant Life Management, Shanghai (2007).

[4] A Physically Based Correlation of Irradiation-Induced Transition Temperature Shifts for RPV Steels, E.D. Eason, G.R. Odette, R.K. Nanstad, T. Yamamoto, Oak Ridge, 2006.

[5] AMERICAN SOCIETY FOR TESTING AND MATERIALS, ASTM E521, Standard Practice for Neutron Radiation Damage Simulation by Charged Particle Irradiation, Annual Book of ASTM Standards, ASTM International, West Conshohocken, PA (2002).

[6] IAEA Nuclear Energy SeriesTechnical, No. NP-T-3.11, Integrity of Reactor Pressure Vessels in Nuclear Power Plants: Assessment of Irradiation Embrittlement Effects in Reactor Pressure Vessel Steels, VIENNA (2009).

[7] Embrittlement of Nuclear Reactor Pressure Vessels, G.R. Odette, G.E. Lucas, JOM, 53 (7) (2001), pp. 18-22.

[8] Flux Effects and the Prediction of Embrittlement at High Fluence, IAEA Regional Workshop on Structure, Systems and Components Integrity, Randy K. Nanstad, Belo Horizonte, Brazil (2009).

[9] Studsvik Report, Surveillance Testing of Ringhals 3 and 4 Reactor Pressure Vessel, STUDSVIK/N-07/061, Kjell Noring (2007).

[10] Swedish State Power Board: Ringhals Unit no.3 Reactor Vessel Radiation Surveillance Program, 1977.

[11] The Engineering Institution for Welding and Joining Professionals, http://www.twiprofessional.com/content/jk71.html

[12] A REVIEW OF FORMULAS FOR PREDICTING IRRADATION EMBRITTLEMENT OF REACTORS VESSEL MATERIALS, EUR 16455 EN, AMES Report No.6, Pierre Petrequin, Paris (1996).

[13] Assessment and Management of Ageing of Major Nuclear Power Plant Components Important to Safety: PWR Pressure Vessels, 2007 Update, IAEA-TECDOC-1556, Vienna, 2007.

[14] State of the Art on Role of Nickel and Manganese on Radiation Embrittlement, EUR 21304 EN, L. Debarberis, B. Acosta, F. Sevini, 2003.

[15] Effects of Residual Elements on Predicted Radiation Damage to Reactor Vessel Materials, Regulatory Guide 1.99, Rev 1, U.S. Nuclear Regulatory Commision, Washington D.C., 1977.

[16] Radiation Embrittlement of Reactors Vessel Materials, Regulatory Guide 1.99, Rev 2, U.S. Nuclear Regulatory Commision, Washington D.C., 1998 .

[17] A Comparison between French Surveillance Program Results and Predictions of Irradiation Embrittlement, Influence of Radiation on Materials Properties: 13th International Symposium, ASTM STP 956, C. Brillaud, F. Hedin, B. Houssin, Philadelphia, 1987.

[18] The Nil-ductility Temperature Shift Arising from Irradiation as Predicted through the French Test Reactors Experiments, Effects of Radiation on Materials: 14th International Symposium, Vol. II, ASTM STP 1046, D. Miannay, D. Dussartè, P. Soulat, Philadelphia, 1990.

[19] Safety Standards of the Nuclear Safety Standards Commision (KTA), KTA 3203, Surveillance of the Irradiation Behaviour of Reactor Pressure Vessel Materials of LWR Facilities, Salzgitter (2001).

[20] Guidelines for prediction of irradiation embrittlement of operating WWER-440 reactor pressure vessels, IAEA-TECDOC-1442, Vienna, 2005.

[21] Extended analysis of VVER-1000 surveillance data, A. Kryukov, D. Erak, L. Debarberis, F. Sevini, B. Acosta, International Journal of Pressure Vessels and Piping 79, (2002).

[22] PERFECT: "Prediction of Irradiation Damage Effects on Reactor Components", J-P. Massoud, S. Bugat, J-L. Boutard, D. Lidbury, S. Van Dyck, F. Sevini.

[23] PERFECT official website, https://fp6perfect.net/site/index.htm

[24] A Comparison of the tanh and Exponential Fitting Methods for Charpy V-Notch Energy Data, Journal of Pressure Vessel Technology Vol. 131, 031404-1, 2009.

[25] Studsvik Report, Surveillance Testing of Ringhals 2 Reactor Pressure Vessel, STUDSVIK/N-07/060, Kjell Noring (2007).

A Appendix - Model Comparison

Figure 11 shows the Reg.G.Rev.1, FIM and Miannay formulas, compared to the measured data for all shell courses. The following pictures include all models.

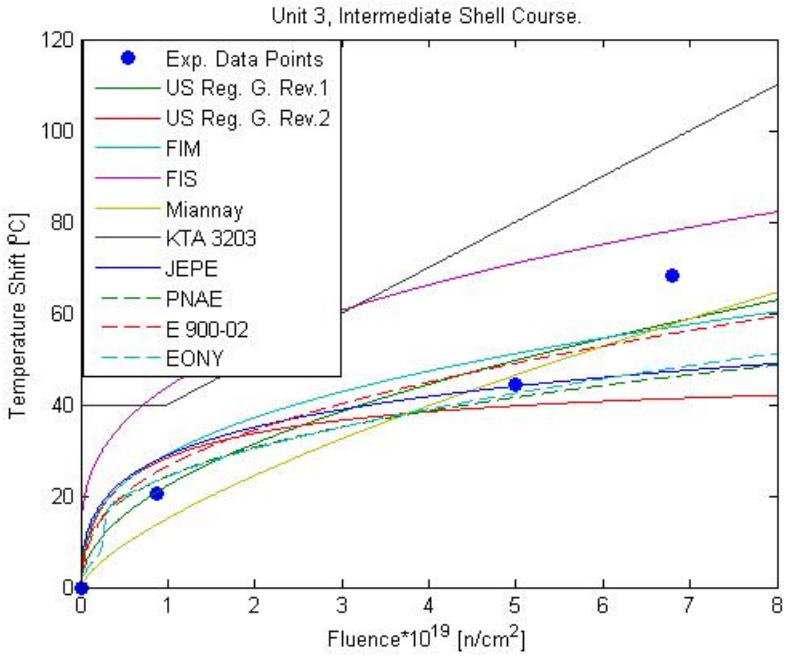

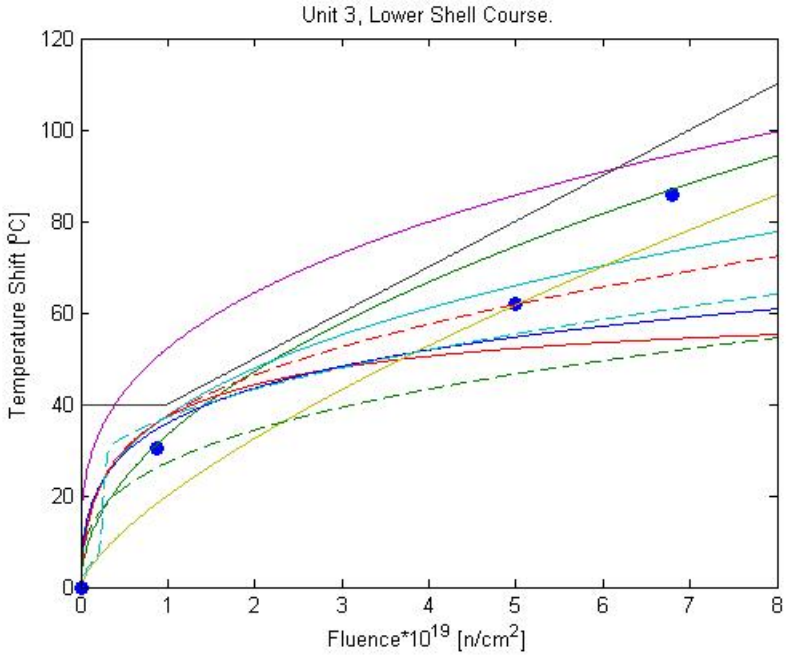

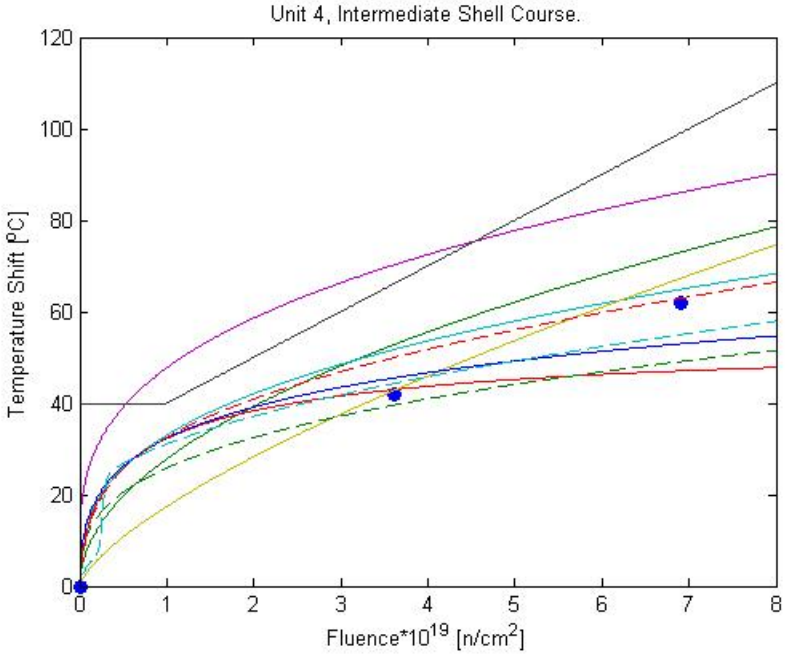
Unit 4, Intermediate Shell Course.
Temperature Shift [°C]
Fluence*10^19 [n/cm^2]
0
20
40
60
80
100
120
0
1
2
3
4
5
6
7
8

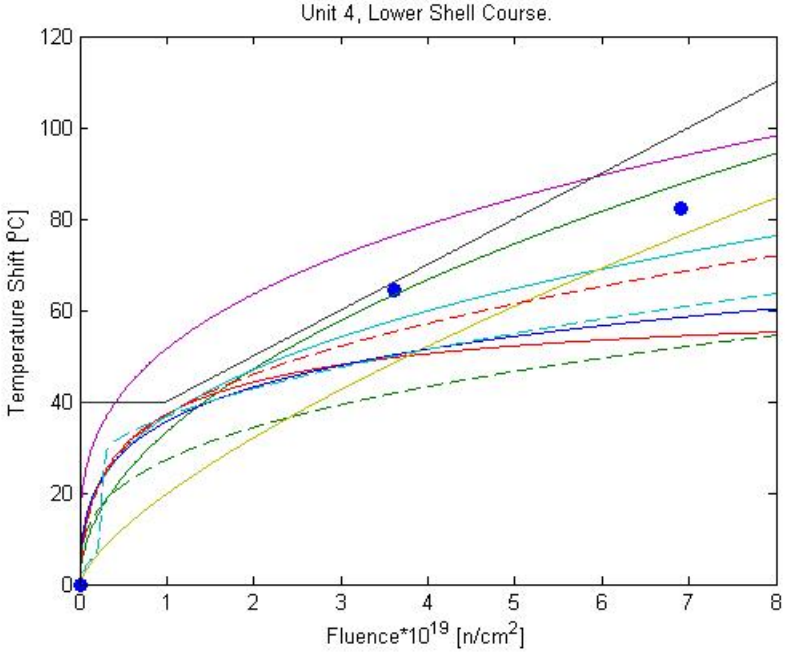
Unit 4, Lower Shell Course.
Temperature Shift [°C]
Fluence*10^19 [n/cm^2]
0
20
40
60
80
100
120
0
1
2
3
4
5
6
7
8

B Appendix - Chemical Analysis

B.1 Analysis of linear elemental terms

B.1.1 Correlations between $\Delta T/\phi^{0.52}$ and chemical contents

Figure 14 shows $\Delta T/\phi^{0.52}$ for Cu and Mn, considering the base metal data. Here follows corresponding figures for all elements investigated.

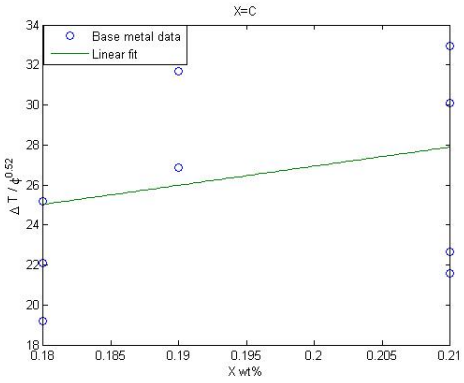

(a) $X = C$.

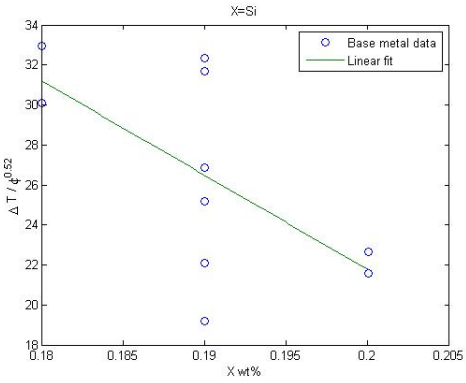

(b) $X = Si$.

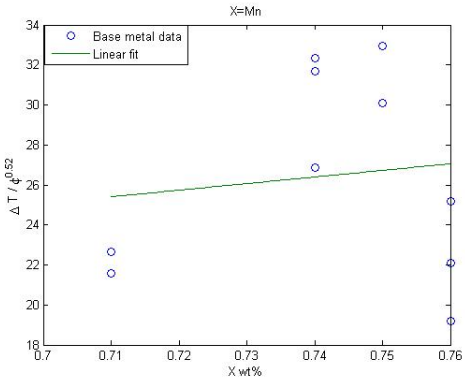

(c) $X = Mn$.

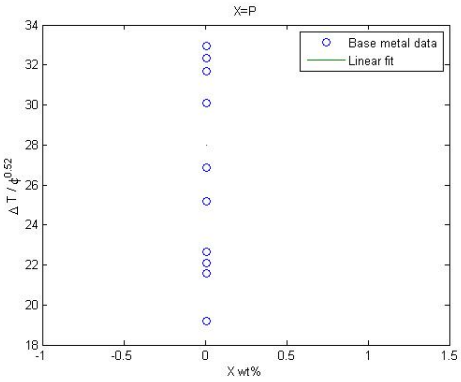

(d) $X = P$.

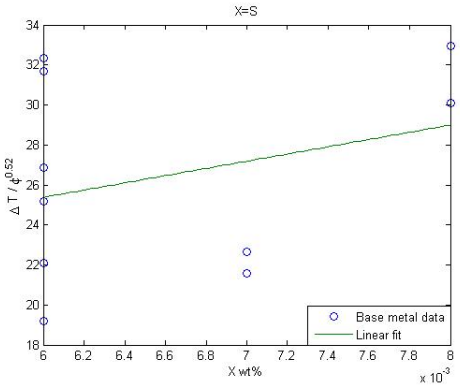

(e) $X = S$.

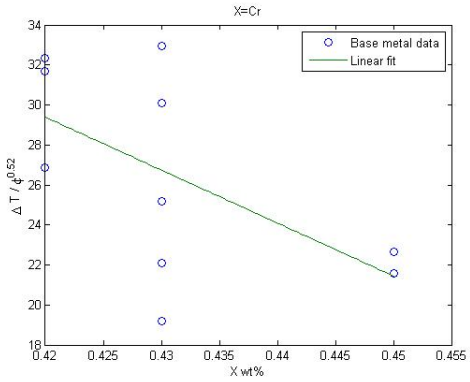

(f) $X = Cr$.

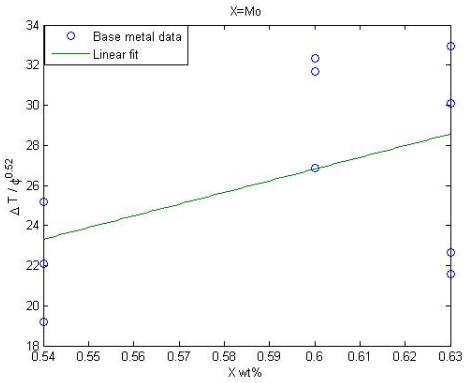

(g) $X = Mo$.

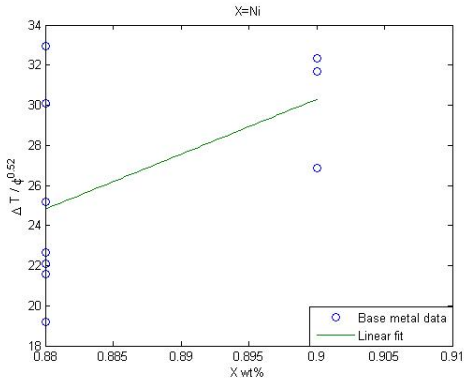

(h) $X = Ni$.

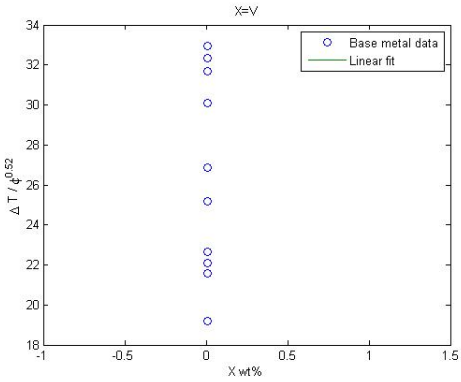

(i) $X = V$.

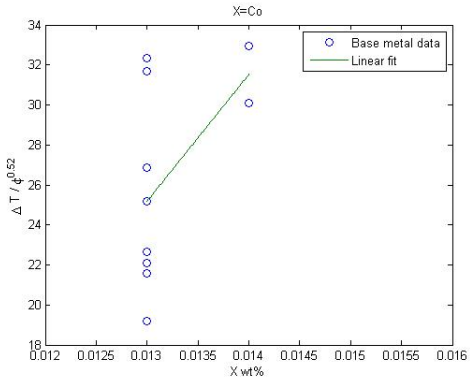

(j) $X = Co$.

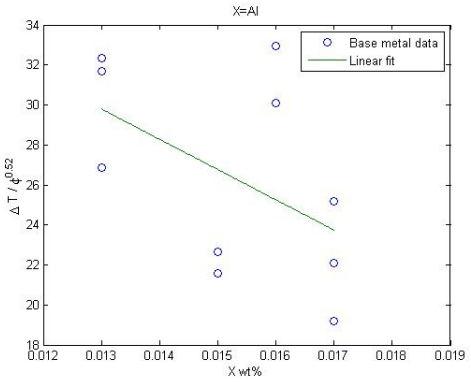

(k) $X = Al$.

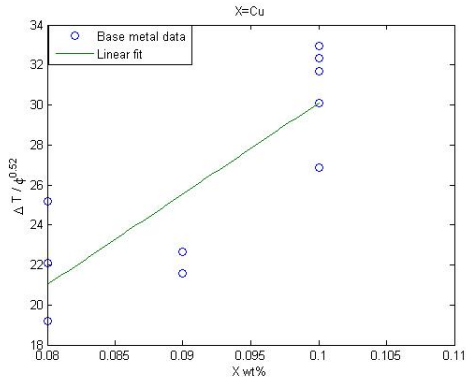

(l) $X = Cu$.

Figure 24: Temperature shifts with fluence dependence removed, as function of chemical contents. Linear fits are included.

Regarding the linear fits included, only Cu displays an increasing behavior with 95% certainty. For no other element can $\Delta T/\phi^{0.52}$ be taken to linearly increase or decrease with the same probability. For some of the elements included there is no variation in wt%'s, i.e. P and V.

B.1.2 Graphical presentation of equation (19)

Here all graphical representations considering elemental parameters, X or $X \cdot Y$ and Z, as in (19) (i.e. $\Delta T = (418Cu + \alpha X + const)\phi^{0.52}$), are shown. Both base- and weld-metal data are used for the following figures. The elements and sums of model residuals are seen in table 11.

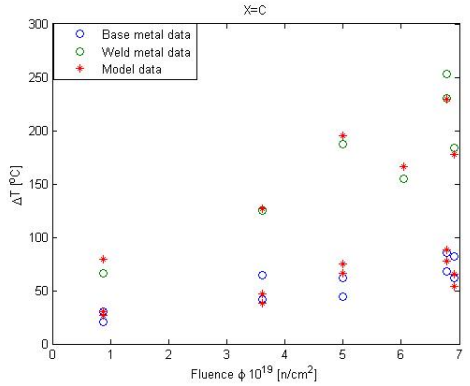

(a) $X = C$.

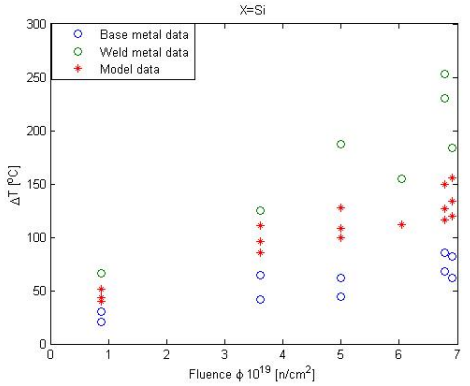

(b) $X = Si$.

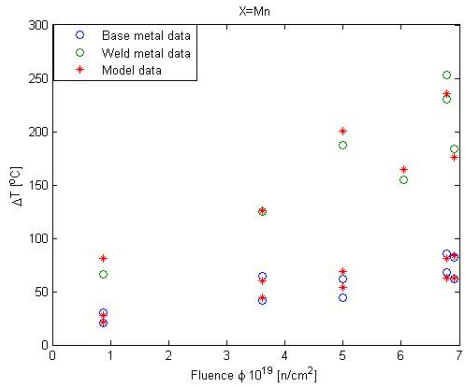

(c) $X = Mn$.

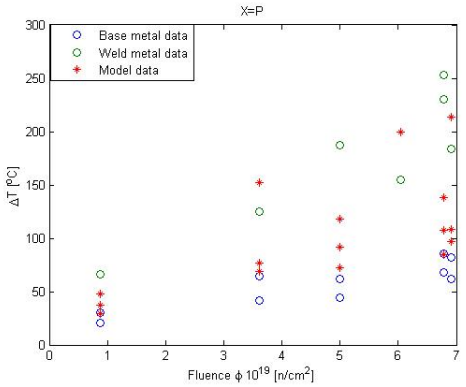

(d) $X = P$.

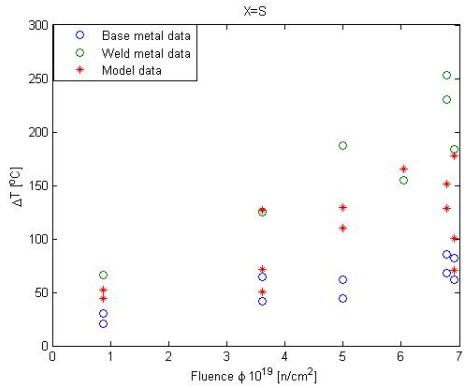

(e) $X = S$.

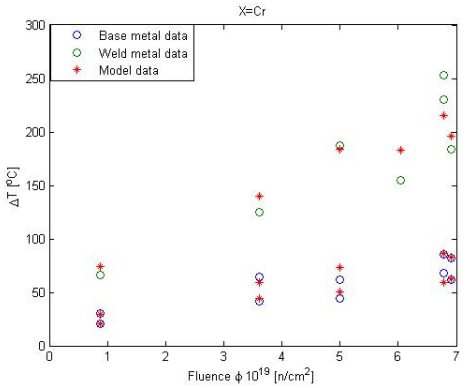

(f) $X = Cr$.

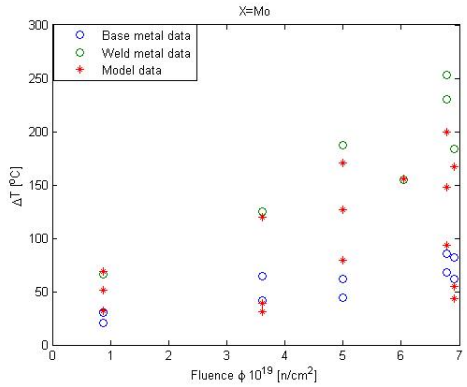

(g) $X = Mo$.

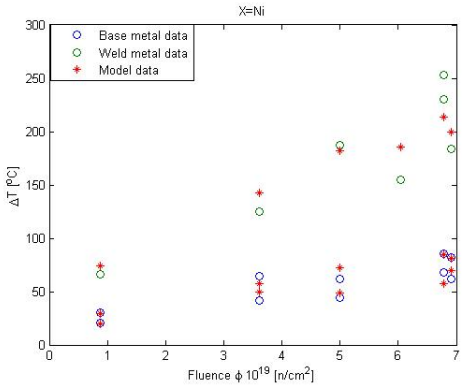

(h) $X = Ni$.

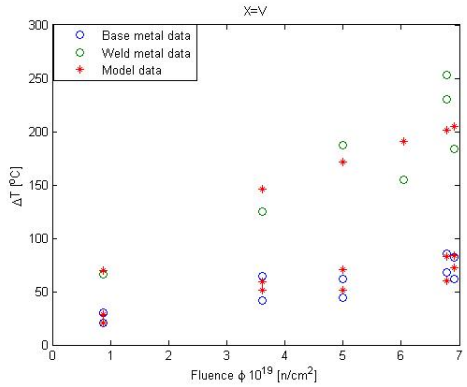

(i) $X = V$.

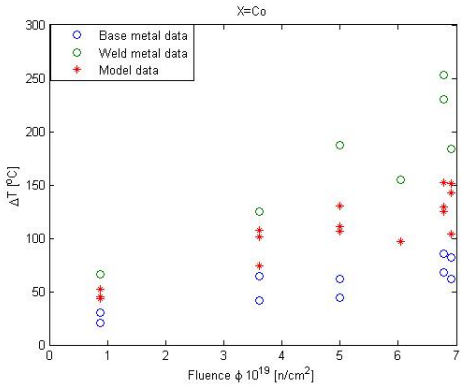

(j) $X = Co$.

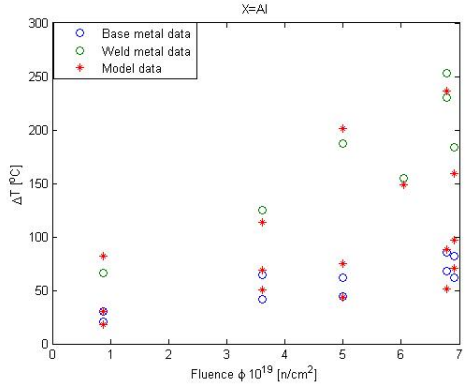

(k) $X = Al$.

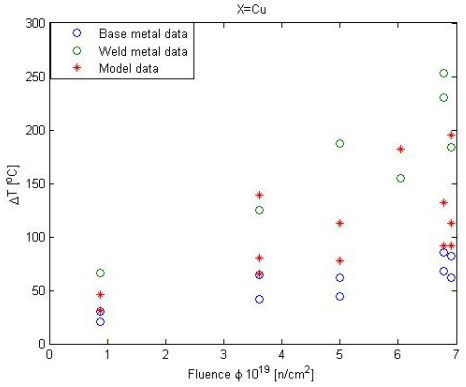

(l) $X = Cu$.

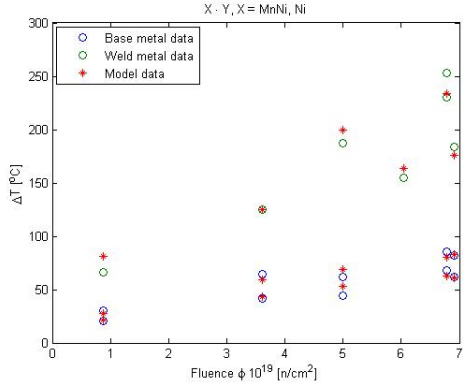

(m) $X \cdot Y, Z = MnNi, Ni$.

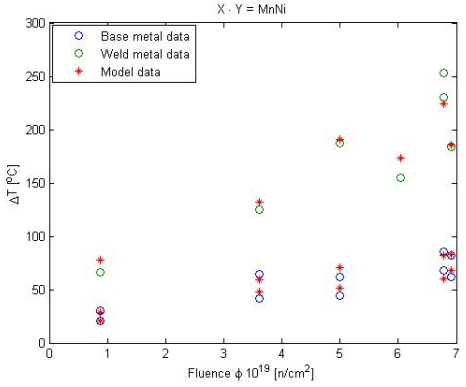

(n) $X \cdot Y = MnNi$.

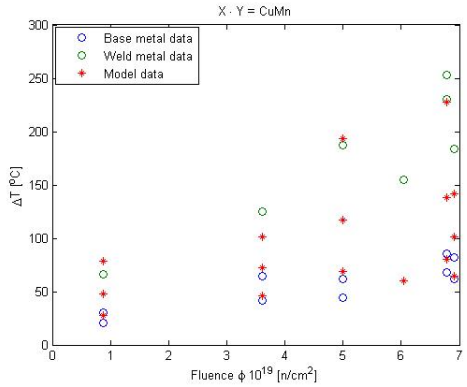

(o) $X \cdot Y = CuMn$.

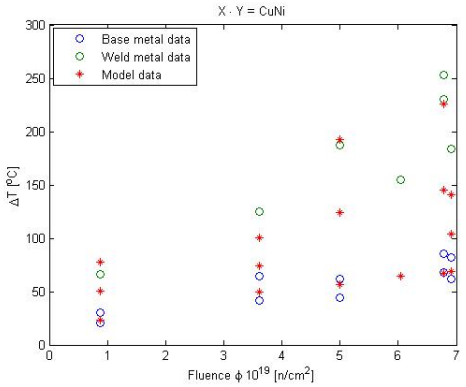

(p) $X \cdot Y = CuNi$.

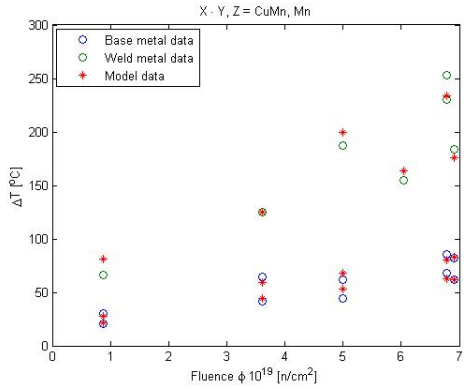

(q) $X \cdot Y, Z = CuMn, Mn$.

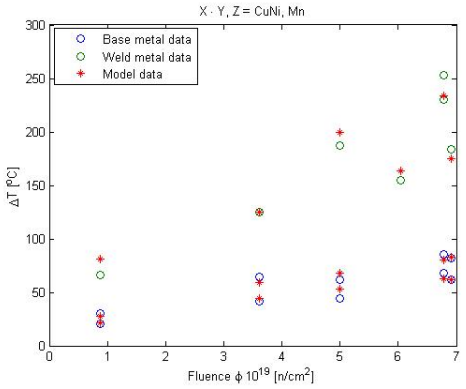

(r) $X \cdot Y, Z = CuNi, Mn$.

Figure 25: Fitted models with linear dependance on Cu and chemical parameter X, or $X \cdot Y$ and Z.

For elements where no real trend in chemical contents between weld- and base-metals is apparent (i.e. no distinction comparing base and weld), the models will be minimized to an "average" between all measured points. This is particularly clear for Si and Co. It is also apparent, observing $X = Cu$, that Cu alone is not sufficient for explaining temperature shifts in both base- and weld-metals. Furthermore, the Cu-coefficient will in this case be negative, clearly contradictory to theory.

B.2 Analysis of residuals

In this section the residuals between (20) and measured data points, as functions of elemental parameters X and a number of selected synergistic parameters $X \cdot Y$, are displayed.

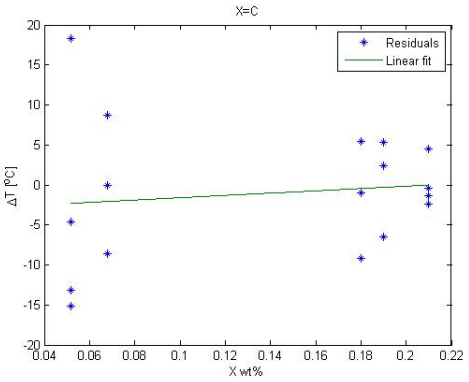

(a) $X = C$.

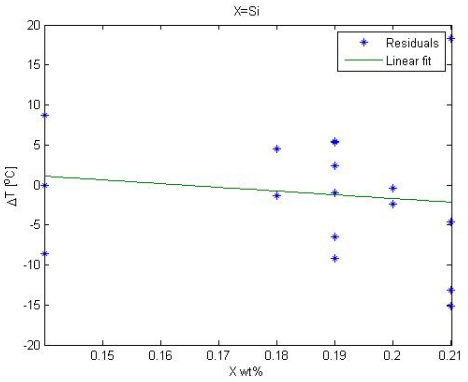

(b) $X = Si$.

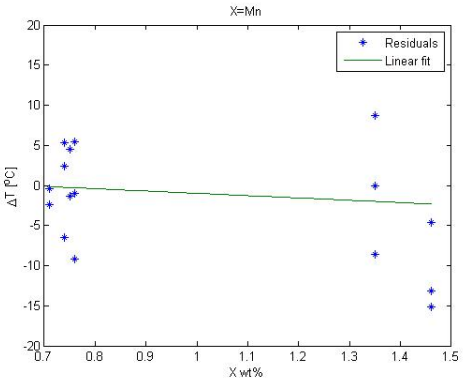

(c) $X = Mn$.

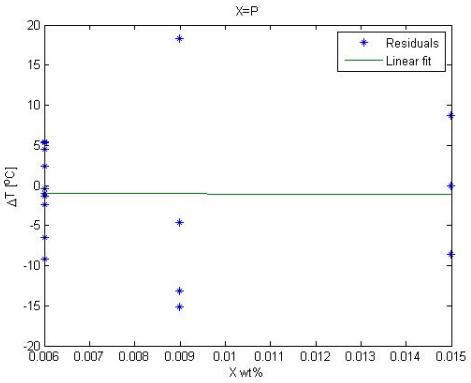

(d) $X = P$.

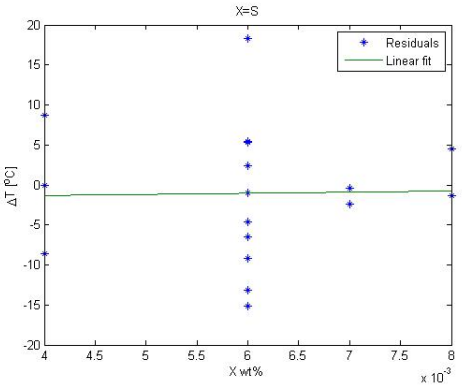

(e) $X = S$.

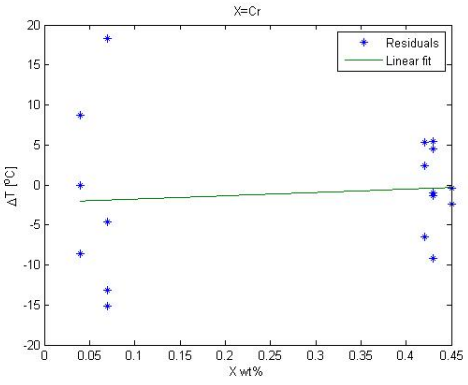

(f) $X = Cr$.

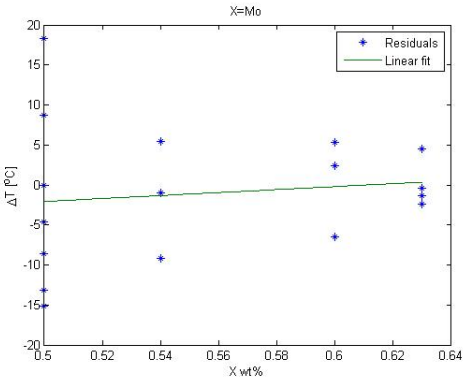

(g) $X = Mo$.

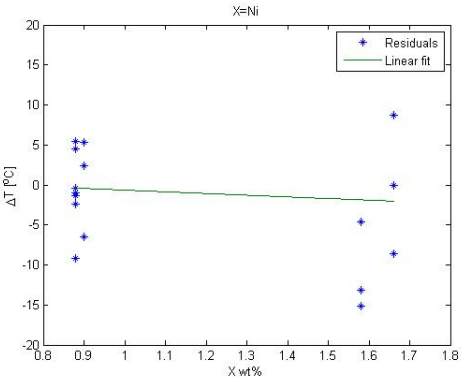

(h) $X = Ni$.

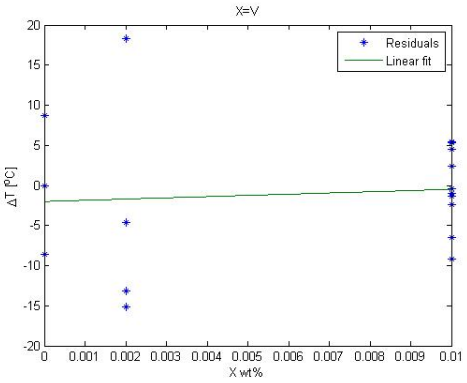

(i) $X = V$.

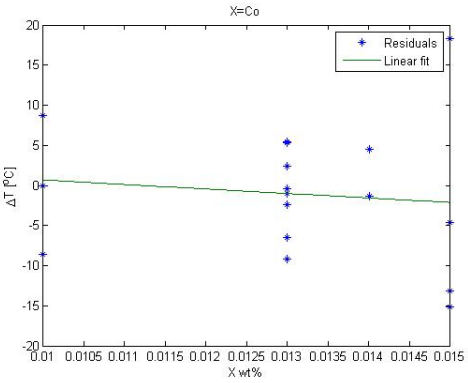

(j) $X = Co$.

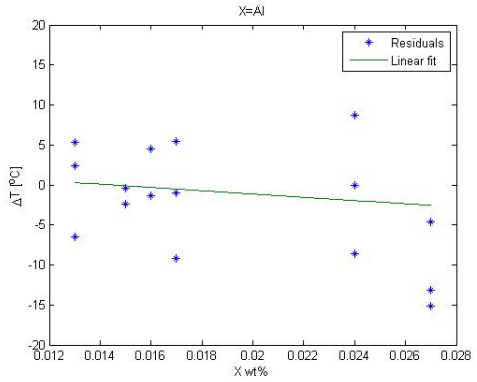

(k) $X = Al$.

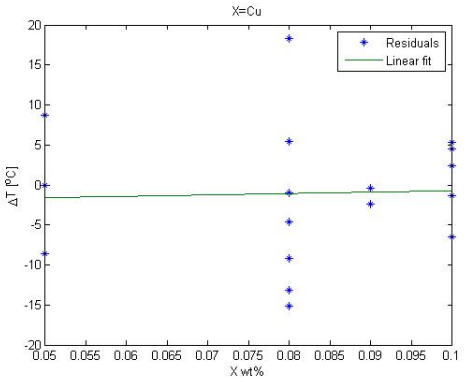

(l) $X = Cu$.

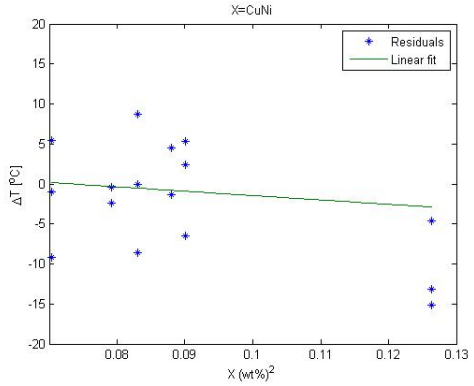

(m) $X = CuNi$.

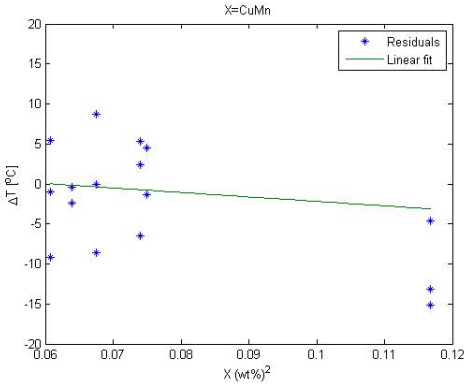

(n) $X = CuMn$.

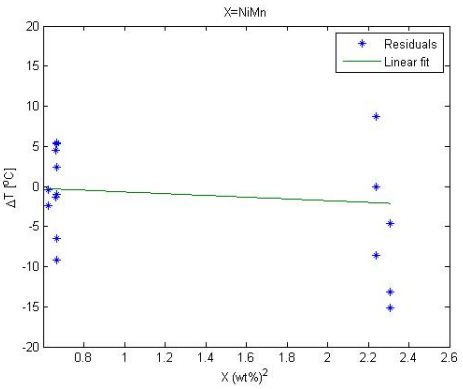

(o) $X = NiMn$.

Figure 26: Residuals vs. chemical contents (X wt %, or $X \cdot Y$ (wt %)^2). Also included are linear fits.

Although the slope of some linear fits appear to suggest a decreasing/increasing behavior, no such dependencies are certain within a 95% confidence bounds.